MECHANICAL BEHAVIOR OF MEDIUM AND HIGH ENTROPY ALLOYS

2024
MASTER THESIS
MECHANICAL ENGINEERING

Ahmad MADKHANAH

Thesis Advisor
Assist. Prof. Dr. Sezer PIÇAK

MECHANICAL BEHAVIOR OF MEDIUM AND HIGH ENTROPY ALLOYS

Ahmad MADKHANAH

Thesis Advisor
Assist. Prof. Dr. Sezer PIÇAK

T.C.
Karabük University
Institute of Graduate Programs
Department of Mechanical Engineering
Prepared as
Master Thesis

KARABÜK
July 2024

I certify that in my opinion the thesis submitted by Ahmad MADKHANAH titled "MECHANICAL BEHAVIOR OF MEDIUM AND HIGH ENTROPY ALLOYS" is fully adequate in scope and in quality as a thesis for the degree of Master of Science.

Assist. Prof. Dr. Sezer PIÇAK ....
Thesis Advisor, Department of Mechanical Engineering

This thesis is accepted by the examining committee with a unanimous vote in the Department of Mechanical Engineering as a Master of Science thesis. July 16, 2024

Title, Name SURNAME (Institution) Signature

Chairman : Assist. Prof. Dr. Sezer PIÇAK (KBU) ....

Member : Assoc. Prof. Dr. Okan ÜNAL (KBU) ....

Member : Assoc. Prof. Dr. Nafiz YAŞAR (DPU) ....

The degree of Master of Science by the thesis submitted is approved by the Administrative Board of the Institute of Graduate Programs, Karabük University.

Assoc. Prof. Dr. Zeynep ÖZCAN ....
Director of the Institute of Graduate Programs

Ahmad MADKHANAH

ABSTRACT

Master Thesis

MECHANICAL BEHAVIOR OF MEDIUM AND HIGH ENTROPY ALLOYS

Ahmad MADKHANAH

Karabük University
Institute of Graduate Programs
Department of Mechanical Engineering

Thesis Advisor:
Assist. Prof. Dr. Sezer PIÇAK
July 2024, 75 pages

Medium- and high-entropy alloys (M/HEAs) provide a vast and diverse design space compared to traditional alloys, creating new opportunities for uncovering un-explored physics and functionalities. Some of these alloys demonstrate an excep-tional combination of high strength and ductility, which has been attributed to the activation of multiple deformation mechanisms initiated by low- and medium-energy stacking faults. Despite numerous recent studies investigating the micro-scopic and macroscopic properties of these materials, research on single crystalline M/HEAs is notably lacking. Such studies are crucial for gaining a deeper under-standing of the fundamental deformation mechanisms. In response to this gap, the current study focuses on fabricating and characterizing single and polycrystalline M/HEAs to explore the underlying deformation processes responsible for their re-markable mechanical behavior.

In this work, the tensile deformation behavior of NiCoCr single crystals was studied along different crystallographic orientations, including [001], [011] and [111]. Detailed microstructural analyses were carried out to identify the dominant mecha-nisms during deformation and compared with the existing literature. Through ex-tensive characterization of bulk single crystals, it was found that the exceptional mechanical properties of NiCoCr result from short-range atomic order (SRO). This SRO promotes the simultaneous activation of twinning-induced plasticity (TWIP) and transformation-induced plasticity (TRIP), which leads to dynamic hardening by restricting dislocation motion through the formation of nanoscale twin and marten-site boundaries. These findings suggest that the interaction between SRO and plas-ticity can be harnessed to activate various deformation mechanisms, potentially leading to the discovery of new M/HEAs with unprecedented mechanical proper-ties.

Keywords : High entropy alloys, Microstructure, Slip, Single crystals, Short-range ordering, Interstitial, Strain hardening, Twinning, Martensitic transformation.
Science Code : 91421

ÖZET

Yüksek Lisans Tezi

ORTA VE YÜKSEK ENTROPİLİ ALAŞIMLARIN MEKANİK DAVRANIŞI

Ahmad MADKHANAH

Karabük Üniversitesi
Lisansüstü Eğitim Enstitüsü
Makine Mühendisliği Anabilim Dalı

Tez Danışmanı:
Dr. Öğr. Üyesi Sezer PIÇAK
Temmuz 2024, 75 sayfa

Orta ve Yüksek Entropili Alaşımlar (M/HEA'lar), geleneksel alaşımlara kıyasla geniş ve çeşitli bir tasarım alanı sunarak keşfedilmemiş fiziksel özellikler ve fonksiyonellikler için yeni fırsatlar yaratmaktadır. Bu alaşımların bazıları, düşük ve orta enerjili yığılma hataları ile başlatılan birden fazla deformasyon mekaniz-masının etkinleşmesine bağlı olarak olağanüstü bir yüksek mukavemet ve süneklik kombinasyonu sergilemektedir. Bu malzemelerin mikroskobik ve makroskobik özelliklerini inceleyen birçok güncel çalışmaya rağmen, tek kristalli M/HEA'lar üzerine yapılan araştırmalar dikkate değer şekilde eksiktir. Bu tür çalışmalar, temel deformasyon mekanizmalarını daha derinlemesine anlamak için büyük önem taşımaktadır. Bu eksikliğe yanıt olarak, mevcut çalışma, M/HEA'ların tek ve çok kristalli örneklerini üretmeye ve karakterize etmeye odaklanarak, bu malzemelerin dikkate değer mekanik davranışlarından sorumlu temel deformasyon süreçlerini araştırmayı amaçlamaktadır.

Bu çalışmada, NiCoCr tek kristallerinin farklı kristalografik yönelimlerdeki [001], [011] ve [111] boyunca çekme deformasyon davranışı incelenmiştir. Deformasyon sırasında baskın mekanizmaları belirlemek için ayrıntılı mikroyapı analizleri yapılmış ve mevcut literatür ile karşılaştırılmıştır. Yapılan kapsamlı tek kristal karakterizasyonu sonucunda, NiCoCr'nin olağanüstü mekanik özelliklerinin, atom-ların kısa menzilli düzenlenmesinden (SRO) kaynaklandığı bulunmuştur. Bu SRO, dislokasyon hareketini nanoskopik ikiz ve martenzit sınırlarının oluşumu yoluyla kısıtlayarak, ikizlenme kaynaklı plastiklik (TWIP) ve dönüşüm kaynaklı plastiklik (TRIP) mekanizmalarının eşzamanlı olarak etkinleşmesini sağlamaktadır. Bu bul-gular, SRO ile plastiklik arasındaki etkileşimin çeşitli deformasyon mekanizma-larını etkinleştirmek için kullanılabileceğini ve bu sayede benzeri görülmemiş mekanik özelliklere sahip yeni M/HEA'ların keşfine olanak tanıyabileceğini göstermektedir.

Anahtar Sözcükler : Yüksek entropili alaşımlar, Mikroyapı, Kayma, Tek kristaller, Kısa menzilli düzen, Arayer atomlar, Deformasyon sertleşmesi, İkizlen-me, Martenzit dönüşümü.

Bilim Kodu **:** 91421

ACKNOWLEDGEMENT

I would like to express my deepest gratitude to everyone who has supported me throughout the process of completing this thesis on the Mechanical Behavior of Medium and High Entropy Alloys.

First and foremost, I am profoundly grateful to my supervisor, Assist. Prof. Dr. Sezer PIÇAK, for their continuous guidance, insightful feedback, and unwavering support. Their expertise in materials science and their dedication to fostering my academic growth have been invaluable throughout this research.

I would also like to extend my appreciation to the faculty and staff of the Mechani-cal Engineering Department, for providing an enriching academic environment and access to the necessary resources and facilities to carry out this work. Special thanks to the laboratory team for their assistance with the experimental procedures and for their patience in addressing my questions during data collection.

I am also deeply thankful to my family and friends for their love, encouragement, and understanding throughout this journey. Their belief in me has been a source of strength.

TABLE OF CONTENTS

Page

APPROVAL ii

ABSTRACT iv

ÖZET vi

ACKNOWLEDGEMENT viii

TABLE OF CONTENTS ix

LIST OF FIGURES xi

LIST OF TABLES xiv

SYMBOLS AND ABBREVITIONS INDEX xv

CHAPTER 1 1

INTRODUCTION 1

- 1.1. MOTIVATION AND SIGNIFICANCE OF WORK 1
- 1.2. BACKGROUND 3
  - 1.2.1. The Effect of Stacking-Fault Energy on Mechanical Properties 6
  - 1.2.2. Short-range Ordering in Medium and High Entropy Alloys 11
  - 1.2.3. Strain Hardening Behavior of Medium/High Entropy Alloys 19
  - 1.2.4. Interstitial Effect on Mechanical Properties of M/HEAs 21
  - 1.2.5. Plastic Deformation in Single Crystals: 26
  - 1.2.6. Manufacturing Techniques of Single Crystals 27
  - 1.2.7. Polycrystalline M/HEAs 35
  - 1.2.8. Non-monotonic Loading and Fatigue Lives of M/HEAs 36
- 1.3. OBJECTIVES AND OUTLINE 38

CHAPTER 2 39

EXPERIMENTAL METHODS 39

- 2.1. MATERIALS 39
- 2.2. UNIAXIAL TENSILE TEST RESULTS 40
- 2.3. TRANSMISSION ELECTRON MICROSCOPY 41

Page

CHAPTER 3 42

ON THE ORIGIN OF STRAIN-HARDENING BEHAVIOR OF SINGLE CRYSTALLINE NiCoCr MEDIUM ENTROPY ALLOY 42

3.1. DETECTION OF SHORT-RANGE ORDERING (SRO).......................... 47

3.2. EFFECT OF SHORT-RANGE ORDERING ON THE MECHANICAL PROPERTIES 52

3.3. COMPARISON OF MECHANICAL TENSILE TESTS OF MEDIUM AND HIGH ENTROPY ALLOYS WITH CONVENTIONAL STEELS 54

CHAPTER 4 57

CONCLUSIONS.. 57

REFERENCE... 60

RESUME 75

LIST OF FIGURES

Page

Figure 1. Schematic illustration of Stacking-fault driven deformation twinning and HCP transformation. a) pathway for deformation twinning, FCC into ISF into ESF into twinning. b) HCP transformation pathway, FCC into ISF into HCP [75]. 7

Figure 2. a) Schematic illustration of extrinsic and intrinsic SFs [77]. b) diagonal SFs observed in an FCC Co, in different (111) planes [78]. c) Parallel SFs observed in HCP Co basal plane [79]. d) SFs on basal plane of Mg alloys, hot rolled to 88% strain [80]. e) SFs observed in a nanoscale Ti film [81]. f) Nano-sized SFs in Al0.1CoCrFeNi HEA [82]. g) Dark field TEM image of SFs in Fe50Mn30Co10Cr10 HEA [83]. 9

Figure 3. Bight-field (BF) and dark-field (DF) TEM images of NiCoCr MEA samples subjected to tension up to fracture at RT and 15 K. a) Dislocations and numerous stacking faults, RT sample. b) Deformation twinning and selected-area diffraction (SAD) pattern for further evidence (inset). c) Dislocations and SFs, 15 K sample. d) DF image showing HCP phase with further evidence by SAD pattern (inset). HCP lamellae and SFs. f) HRTEM image of adjacent regions of FCC and HCP [75].......... 10

Figure 4. TEM images of Fe$_{40}$Mn$_{40}$Co$_{10}$Cr$_{10}$ HEA deformed up to failure. a) SF parallelepipeds. b) a SF-twinning interaction. c) zoom-in of the dotted red squared area in b) [84].......... 11

Figure 5. Schematic illustration of random solid solution, short-order and long-range order in a binary system [74].......... 12

Figure 6. Experimental characterization of SRO by a) APT, conducted on an annealed TaNbHfZr HEA, b) energy-filtered diffraction pattern, conducted on NiCoCr MEA. The APT measurements indicate SROs enriched by Zr/Hf [97]. The distinct streaking stems from SRO domains' diffuse scattering signals [22]. 14

Figure 7. STEM-HAADF image with the [112] zone axis, FFT pattern inset. Note that there are extra diffusions at 12311, as well as the sharp Bragg spots from FCC diffraction [102]. 15

Figure 8. EDS mapping from the HAADF image in Figure 7 with zoomed-in maps. White lines mark the intersection between 311 and (111) planes [102]. 15

Figure 9. Investigation of SRO in NiCoCr MEA single crystals in the [001] zone axis using polar synchrotron transmission x-ray diffraction spectra [100]. a) WQ, b) 48h-aged samples. The extra reflections indicating SRO can be seen in both samples (white circles).......... 16

Page

Figure 10. STEM-FFT pattern showing MSRO (left). Inverse FFT pattern created by superimposing a single MSRO domain with FCC lattice fringes (right) [108]. 17

Figure 11. Tensile test results of [111]-, [110]- and [001]-oriented WQ and 48h-aged samples of single crystalline NiCoCr MEA, at 300 K [100]. 18

Figure 12. Local strain maps generated using geometrical phase analysis (GPA) in VNiCo MEA, before (left) and after (right) deformation. The inset on the left illustrates the alternating planes in the SRO. A close-up view of a contrasting local strain can be seen in the inset on the right [110]. 19

Figure 13. a) Illustration of four strain hardening stages of Fe-17%Mn-0.4%C-1.3%Al TWIP steel. b) Enlargement of the area defined indicated in a). σ_T is the twinning stress. The strain hardening rate peaks at the transition from stage II to stage III [111]. 21

Figure 14. XRD analysis of FeCoCrNiMn HEA with varying C concentrations. .. 23

Figure 15. EBSD maps showing the post-fracture microstructure of a) C0 and b) C3.3 samples of the HEA [124]. 23

Figure 16. EBSD maps showing phase distribution of $Fe_{50}Mn_{25}Cr_{15}Co_{10}$, annealed (c1), strained to 10% (c2) and 20% (c3); $Fe_{50}Mn_{25}Cr_{15}Co_{10}N_{1.0}$, annealed (d1), strained to 10% (d2) and 20% (d3); (e1-e3) EBSD phase map of $Fe_{50}Mn_{25}Cr_{15}Co_{10}N_{1.6}$, annealed (e1), strained to 10% (e2) and 20% (e3) [131]. 25

Figure 17. Zone melting. [155]. 28
Figure 18. Power down method schematic [159] 30
Figure 19. Bridgman-Stockbarger Method [161]. 32
Figure 20. LMC Method Schematic [166]. 33
Figure 21. The Czochralski method schematic [173]. 35
Figure 22. Tensile and compressive tests specimens' designs. 40
Figure 23. a) The room temperature engineering stress - engineering strain tension responses of the [111], [110]- and [001]-oriented single crystals of the NiCoCr MEA. The evolution of θ ($d\sigma/d\varepsilon$), with true strain for the b) [111], c) [110] and d) [123]-oriented crystals. Inverse pole figures and 3D schematics inset show the initial loading directions (IPFX) for three orientations, measured using EBSD. The stages of deformation were also marked for each orientation. 43

Figure 24. Representative EBSD ipf color maps illustrate microstructure of single crystalline nicocr samples deformed up to failure. a) the [110]-oriented single crystal deformed up to failure showing the twinning formation, b) ε-martensite, c) the [111]-oriented single crystal deformed up to failure indicating the deformation twinning formation d) ε-martensite. € misorientations maps proving the existence of three different twin systems marked on a). 46

Figure 25. a) X-Ray diffraction analysis of the [111] oriented single-crystal NiCoCr MEA after failure showing additional hcp peak, b) crystallographic

texture analysis of (220) poles for the fcc crystal c) the texture analysis of (1010) poles for the hcp crystal... 47

Figure 26. Bright-field TEM images of the [110]-oriented single crystals after tensile deformation at RT up to 4% strain, showing (b-c) a planar dislocation pile-up on a single slip system with non-equivalent distances between the dislocations at the pile-up tip. 48

Figure 27. The microstructure of water-quenched (WQ, left panel) and 1273 K / 48 h aged (48 h, right panel) samples is shown. (a, b) display energy-filtered diffraction patterns taken along the [110] zone axis for the WQ and 48h samples, respectively. Streaks along the {111} directions are visible only in the 48h sample, as confirmed by the intensity line profile along the dashed lines in the diffraction pattern below. (c, d) show energy-filtered dark-field images of the WQ and 48h samples, with aperture positions marked by blue circles in a) and b). In the 48h sample d), short-range ordered domains (bright dots marked by red circles and blue arrows) ranging from ~2 nm to ~7 nm in size are extensively observed, unlike in the WQ sample. (e, f) present typical high-resolution TEM images and corresponding fast Fourier transform (FFT) images for the WQ and 48h samples. The WQ sample exhibits a mostly uniform structure, while the 48h sample reveals superlattice features (indicated by red circles in f)). Streaking along the {111} directions is also visible in the FFT pattern of the 48h sample f), indicated by blue arrows [100]. 51

Figure 28. Representative EBSD IPF color and phase maps provide a visual overview of the microstructure in single-crystalline NiCoCr specimens. In a), the [111]-oriented, and in b), the [110]-oriented single crystals are shown in their initial as-quenched conditions, deformed to failure, illustrating the formation of twinning and ε-martensite. For the 48-hour aged samples, also deformed to failure, an increased density of twins and ε-martensite is observed. c) displays the corresponding inverse pole figures for the [111]- and [110]-oriented crystals shown in a) and b) [100]. 53

Figure 29. Comparison of the strain hardening rate responses of $Fe_{40}Mn_{40}Cr_{10}Co_{10}$ HEA, Hadfield steel and SS316 stainless steel, obtained from uniaxial tension at room temperature [84]. 54

Figure 30. The comparison of strength differentials (σ - σ_0, where σ_0 is the yield strength) and hardening response as a function of applied strain is shown for three medium to low stacking fault energy materials: 316 stainless steel (SS316) [28], Fe-12%Mn-1%C Hadfield steel [21], and the current medium entropy NiCoCr alloy. This comparison highlights the superior ductility and strength differential of the NiCoCr alloy, which demonstrates a more pronounced hardening response and better mechanical performance compared to SS316 and Hadfield steel under similar strain conditions [3]... 55

LIST OF TABLES

Page

Table 1. SFEs for different deformation mechanisms. 4
Table 2. Schmid factors for slip and twinning in [001], [111] and [123] directions for tension and compression. 27

SYMBOLS AND ABBREVITIONS INDEX

ABBREVIATIONS

ASTM : American Society for Testing and Materials
BSE : Backscattered Electron
CDR : Cyclic Deformation Response
CG : Coarse Grained
CRSS : Critical Resolved Shear Stress
DSA : Dynamic Strain Aging
EBSD : Electron Backscatter Diffraction
ECAP : Equal Channel Angular Pressing
EDM : Electrical Discharge Machining
HEA : High Entropy Alloy
HCF : High-Cycle Fatigue
HDDW : High Density Dislocation Wall
HPT : High Pressure Torsion
HRTEM: High Resolution Transmission Electron Microscopy
LCF : Low Cycle Fatigue
MEA : Medium Entropy Alloy
MPEA : Multi-Principal Element Alloy
SEM : Scanning Electron Microscopy
SFE : Stacking Fault Energy
SPD : Severe Plastic deformation
TEM : Transmission Electron Microscopy
XRD : X-ray Diffraction
FCC : Face Centered Cubic
CRSS : Critical Resolved Shear Stress
m_{slip} : Schmid Factor for Slip
$m_{twinning}$: Schmid Factor for Twinning

CHAPTER 1

INTRODUCTION

This section includes the major properties of medium and high entropy alloys (M/HEAs) to declare the motivation of the current study. The research essentials are discussed after a reviewof research efforts spent on studying this class of material. Eventually, the work objectives and outline will be stated at the end of this chapter.

1.1. MOTIVATION AND SIGNIFICANCE OF WORK

Metals, out of all other elements, have gained an enormous well-deserved interest for ages, due to their essential need in a variety of fields. In spite of that, there always have been some economical and environmental apprehensions that limit their use [1,2]. For centuries, mankind has been striving to alter materials properties through alloying in metallic systems, in order to overcome the challenges and go beyond the limits. Usually, a principal element comprises anotherelement in small percentages, and that has been the case ever since the beginning of alloying, i.e., the Bronze Age. For instance, the composition of conventional steels is made up of primarily iron, combined with small amounts of carbon for strength, and chromium for corrosion resistance. However, this approach needed to be revised in order to overstep its limits. Therefore, efforts havebeen spent towards finding new alloy designs with higher potential and better strength-ductility combinations, as both are desired in structural applications.

In the past two decades, the discovery of a new class of alloys consisting of multi-principal elements, i.e., multi-principal elemental alloys (MPEAs), with at least 3 primary elements, has provided much wider space for compositional design, and opened up an opportunity for the development of new properties, extending the visions for alloying strategies and attractingexaggeratedly rising attention within the science community. Recently developed MPEAs have been shown to possess remarkably superior properties, as compared to conventional alloys, such as strength [3], fracture toughness [4], corrosion and oxidation resistance [5,6], as well as magneticproperties [7]. Due to this set of outstanding properties, MPEAs have gained much interest in the scientific community. MPEAs are also called medium and high entropy alloys (M/HEAs), due totheir high mixing entropies.

HEAs have four main characteristics in common: High levels of entropy, high lattice distortion, sluggish diffusion, and cocktail effects [8], which differ them from other ordinary alloys [9]. The deviation in atomic sizes of solid atoms results in lattice distortion, which contributes to their high strength [10]. Moreover, it impedes atomic movement, reducing the diffusion rate (sluggish diffusion) [11]. The cocktail effect comes from incorporation of multi-principal elements, and thus they have been considered -at the atomic scale- as a composite material [12]. The alloy properties can be adjusted through modulating element types, e.g., using lighter elements results in lower density [13], passive oxide layer forming elements enhance the corrosion resistance [14], etc. At first, it was suggested that the formation of single-phase solid-solution stemmed from the high mixing entropy [11], but later on, evidence [15–18] have shown that this explanation was not enough, since HEAs and MEAs may exhibit local chemical short-range order (SRO) [19–22]. It was also proposed that entropy maximization was always beneficial [4,9,11,23] and this potent mechanical behavior of M/HEAs was a result of solid solution strengthening, as random distribution of constituent atoms impedes dislocation motion, proposed to be proportional to lattice misfit [24]. However, recent findings show that reducing the mixing entropywhich results in producing a dual-phase solid-solution ends up being advantageous in two main aspects: Interface hardening (due to thermal stability being reduced in the high-temperature phase),and transformation-induced plasticity (due to mechanical stability being reduced in the room- temperature phase) [25–29]. Furthermore, neutron scattering based studies [30] have recently concluded that there are no signs of large local lattice distortion in HEAs, which makes the precedingly mentioned solid-solution-focused strengthening theory questionable.

Despite the unique ductility of M/HEAs, their use in engineering applications is restricteddue to lower strength. It was shown recently that increasing the strength at the expense of ductility can be effectively achieved through martensitic transformation [1,31,32], deformation twinning [33,34] as well as precipitation strengthening [31,32]. This results in one of the best hardening combinations, the enormous solid-solution strengthening achieved by combining multi-principal elements in HEAs [1,35], which lead to inter-grain slip resistance, along with the transformation-induced plasticity (TRIP), which is widely known in advanced steels, resulting in further inter- grain slip resistance [36,37]. This simultaneous enhancement in both strength and ductility and this overcome of the so-called strength-ductility trade-off makes TRIP alloys mesmerizing, and discriminates them from other recently developed alloys [38,39].

Dislocation activity, which is considered as a precursor to twinning, has pushed many authors into conducting in-depth studies on the role of slip dislocations in further twin nucleationin low SFE materials, utilizing optical and transmission electron microscopy in result examination [40,41]. The experimental evidence provided in these studies have encouraged researchers to come up with many models for twin nucleation [42,43]. Local stress concentration resulting frommultiple slip dislocation intersection is a common requirement among the precedingly mentionedmodels. However, Mahajan and Chin [44] have proposed a model in which the intersection of multiple slip dislocations resulted in twin nucleation, even though local stress concentration was not observed. Karaman [45] suggests that dislocation pile-up against a barrier in the primary plane is -in most cases- the underlying mechanism behind this stress concentration. Twinning nucleation was reported more frequently in orientations supportive to dislocation pile-up formation, as well as at lower temperatures. Afterwards, twinning continues as a favorable realignment of partial dislocations [45]. The amazing combination of properties mentioned in M/HEAs demand for researches aiming at revealing their underlying secrets, which is the main objective of the present work.

1.2. BACKGROUND

FeNiCoCrMn, the first discovered and in-depth studied HEA, has gained much interest due to its stable single phase fcc crystal structure. The underlying secrets of the extraordinary mechanical behavior of the equiatomic variant of FeNiCoCrMn HEA have recently been reported [4,33,35,46,47]. Many authors have been striving to understand the deformation mechanisms and microstructure evolution of polycrystalline FeNiCoCrMn as per temperature and heat treatment [48,49]. Additionally, researches on single crystals (SCs) of this HEA were conducted to get a better comprehension on the deformation mechanisms with regard to crystallographic orientation [4,48,50–53]. One thing worthy of mentioning is that the stacking fault energy (SFE) of this HEA was reported between 0.018 and 0.027 J/m2, which makes it easier to understand the similarity between its mechanical behavior and that of the low SFE so-called twinning-induced plasticity (TWIP) steels [37,45,54]. According to previous researches, SS316 and SS316L austenitic steels, as well as Hadfield steel (Fe-12Mn-1C) deform by twinning at the onset of plastic deformation in the [111]-oriented crystals when subjected to tension at room temperature, whereas in other orientations it remains absent until the later stages of deformation [45,55,56]. In contrast, deformation twins were rarely observed in FeNiCoCrMn HEA when subjected to tension load at room temperature [48,50], even though TWIP was reported to have a vital effect on the admirable mechanical behavior at cryogenic temperatures [4,48]. Therefore, twinning is considered as a major factor that garnered notice to fcc HEAs due to TWIP effect. The very high levels of strain hardening exhibited by TWIP steels due to twin/twin and twin/slip interactions, which improve ductility by retarding necking instability [37,45,57], are thus almost achievable in HEAs that can undergo deformation twinning. Consequently, many efforts have been aiming at developing low SFE M/HEAs that would behave similar to TWIP steels, and thus, possess extremely high tensile ductility, not only at cryogenic but also at room and higher temperatures [48]. Therefore, SFE is a critical factor that plays a crucial role in alloy designing. Table 1. lists different deformation mechanisms with their SFEs.

Table 1. SFEs for different deformation mechanisms [58–60].

Deformation mechanism	**Dislocation slip**	**Deformation Twinning**	**Twinning and/or Martensitic Transformation**
SFE	≥ 40 mJ/m^2	20-40 mJ/m^2	≤ 20 mJ/m^2

Equiatomic FeMnCoCr (Ni removed variant of the precedingly mentioned alloy) has been reported to have an unfavorable multi-phase microstructure [61]. By reducing the amount of Cr and Co, Deng et al. [28] was able to get rid of the σ phase. SFE can be lowered via reducing the Mn content, as in polycrystalline Fe40Mn40Cr10Co10 HEA, in which deformation response at room temperature is mainly governed by planar slip, until about 10% strain, where twinning starts prevailing gradually [28]. However, this is not the case for all grains, since this HEA displays a strong orientation dependent deformation response. For instance, Deng et al. [28] has reported some grains exhibiting dislocation cell structure, signifying a high SFE material, while high density dislocation walls, planar slip and nano-twins were observed in others, which is the case for low SFE materials. Therefore, there is an urgent demand for a thorough study on SCs of this HEA, in order to understand the underlying mechanisms responsible for this high strain hardening, toughness, and ductility, as a function of crystallographic orientation.

Ever since the discovery of FeMnCoCrNi HEA, many efforts have been spent on developing other quaternary, quinary and ternary fcc, bcc and hcp crystal structured multi- principal elemental alloys [12,61–63]. Researches made on various HEAs and MEAs conclude that NiCoCr MEA has the greatest strength-toughness combination among all other HEAs and MEAs with fcc crystal structure [64,65]. Its relatively low stacking fault energy (SFE) facilitates deformation twinning through reducing the twin formation critical stress [65], delaying the necking instability and enhancing the ductility. This looks feasible when we consider low SFE materials, as they are more susceptible to deformation twinning [3,66], and hence, possess enhanced work hardening rates, ductility and dislocation storage capacity. Similar to TWIP steels [67–69], nanotwins nucleation at the early strain levels promote high strain hardening rates due to the Hall-Petch effect, in which dislocation motion is hindered by twin boundaries [23,64]. Despite the optimistic results acquired on polycrystalline NiCoCr, the microstructural evolution in each individual grain and the corresponding effects are yet to be discovered. For a clearer understanding on the deformation mechanisms corresponding to various individual crystallographic orientations, it is necessary to distinct between grain and twin boundaries effects on the plastic deformation evolution. Consequently, a study on single crystalline NiCoCr focused on determining the different deformation mechanisms and microstructural evolution as a function of crystallographic orientation and strain level is mandatory to the science community.

1.2.1. The Effect of Stacking-Fault Energy on Mechanical Properties

Afar from HEAs, high Mn containing austenitic ferrous alloys are interesting class of materials owing to their high ultimate tensile strength (over 1000 MPa) with over 60% total elongation at room temperature (RT) [45], low/medium stacking fault energies (SFEs), and applications in automotive industry. Several studies were conducted to adjust SFEs of austenitic alloys in order to attain better control over prevailing deformation mechanisms, such as dislocation slip, mechanical twinning, and martensitic transformation [70], which can be extended to those in HEAs. This makes SFE one of the most important factors that dictate the deformation mechanism exhibited by the lattice, as deformation twinning requires a low SFE, as in Hadfield steel. Therefore, tuning SFE plays a critical role in altering mechanical properties in M/HEAs. For example, SFE in $Fe_{40}Mn_{40}Co_{10}Cr_{10}$ HEA can be lowered by the addition of Mn, or totally/partially removing Ni [28]. Getting rid of Ni completely whilst keeping the CoCrFeMnNi HEA at equiatomic composition results in a multiphase microstructure [61]. Thus, in order to avoid the σ phase, Deng et al. [28] reduced the content of Cr and Co in CoCrFeMnNi HEA, which lead to a single phase FCC microstructure. Conversely, an increase in Mn content, particularly in polycrystalline $Fe_{40}Mn_{40}Cr_{10}Co_{10}$ off-stoichiometric HEA, reduces SFE and promotes extreme twinning activity at cryogenic and ambient temperatures. Beside HEAs, many FCC crystal structured MEAs were reported to exhibit such exceptional combination of strength and ductility, particularly NiCoCr and VCoNi MEAs [68,71,72]. Furthermore, NiCoCr exhibits the optimal strength-ductility combination across a broad temperature range [3,4,6]. However, the reasons for this outstanding mechanical behavior are yet to be discovered. The exceptional mechanical behavior in NiCoCr has been attributed to twinning and transformation-induced plasticity (TWIP/TRIP) [71,73]. However, lattice distortion is linked to the extremely high yield strength in VCoNi [74]. Consequently, it is still unclear whether these mechanisms are the primary causes of the unique mechanical behavior. TWIP alloys are often resilient against martensitic transformations, even when they have low SFEs [10]. Therefore, it is uncommon to observe simultaneous TWIP/TRIP at ambient temperatures. Haiyan and co-authors [75] claim that the formation of stacking faults can trigger both deformation twinning and FCC-to-HCP phase transformation, which lead to TWIP and TRIP effects, respectively. According to their claim, there are two pathways with regard to SFs, through which the microstructure goes before eventually exhibiting deformation twinning or HCP phase transformation. The pathways are illustrated in **Error! Reference source not found.** From **Error! Reference source not found.**a, we can see that the microstructure undergoes two main changes before twin nucleation, namely intrinsic and extrinsic stacking faults (ISF and ESF) formation. However, it is possible for the alloy to undergo FCC-to-HCP phase transformation through the formation of intrinsic stacking faults (**Error! Reference source not found.**b). The interesting part here is that we are able to achieve a stacking-fault-driven deformation twinning and/or phase transformation, only through the introduction of Shockley partials. Introducing Shockley partials with burger's vector of $\vec{b} = \frac{1}{6}\langle 11\bar{2}\rangle$ on adjacent (111) planes leads to twin nucleation. Nevertheless, achieving HCP transformation is possible through two sequential ISFs, i.e. two Shockley partials of the same burger's vector on alternating planes.

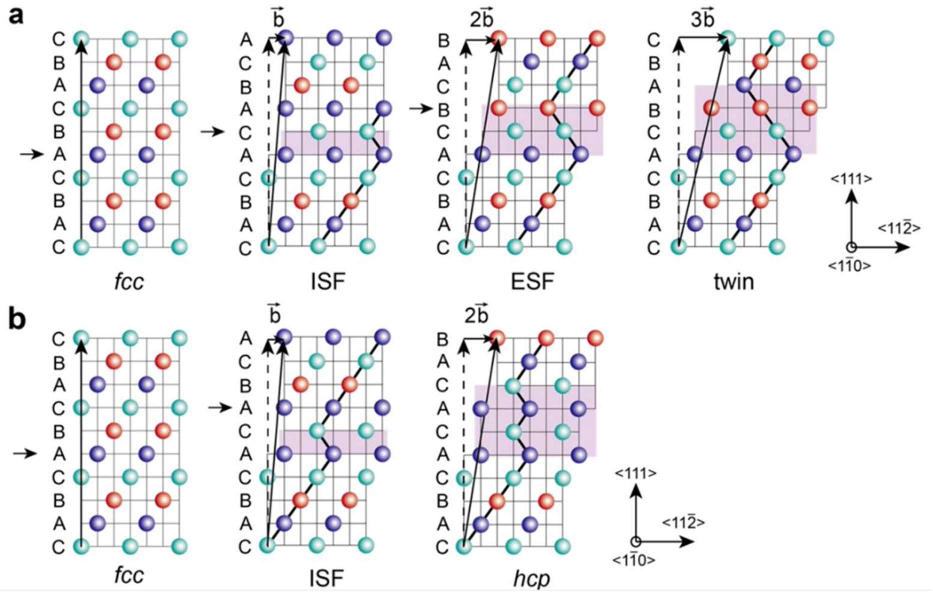

Figure 1. Schematic illustration of Stacking-fault driven deformation twinning and HCP transformation. a) pathway for deformation twinning, FCC into ISF into ESF into twinning. b) HCP transformation pathway, FCC into ISF into HCP [75].

1.2.1.1. Observation and Characterization of SFs

The critical effects of SFs on microstructural evolution and, thus, mechanical behavior, encourages for spending efforts towards microstructural investigation aimed at observing and characterizing SFs. A direct observation of SFs has been reported frequently in the literature.

Su et al. [76] were able to detect SFs directly in TEM images, as well as streaks observed in SAD pattern, as can be seen in Figure 2 These streaks are sometimes confused as indicator of short-range ordering (SRO), which will be discussed in the next section.

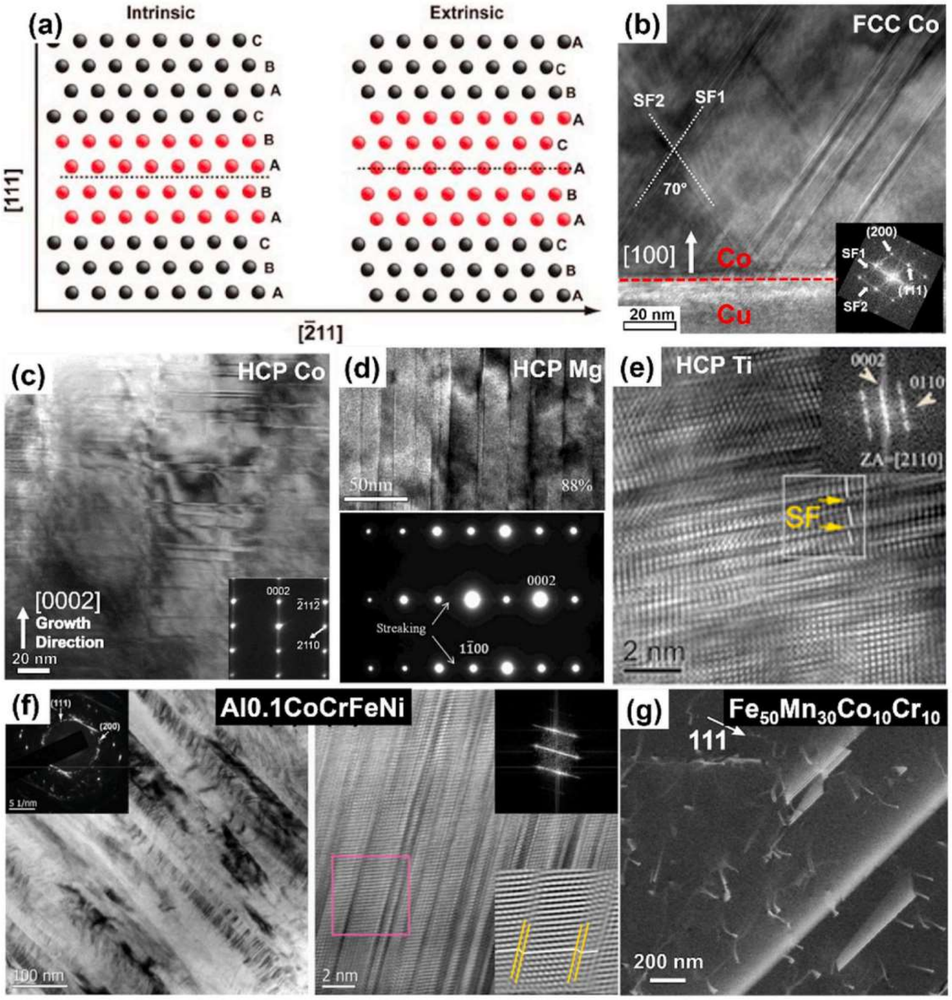

Figure 2. a) Schematic illustration of extrinsic and intrinsic SFs [77]. b) diagonal SFs observed in an FCC Co, in different (111) planes [78]. c) Parallel SFs observed in HCP Co basal plane [79]. d) SFs on basal plane of Mg alloys, hot rolled to 88% strain [80]. e) SFs observed in a nanoscale Ti film [81]. f) Nano-sized SFs in Al0.1CoCrFeNi HEA [82]. g) Dark field TEM image of SFs in Fe50Mn30Co10Cr10 HEA [83].

Using TEM, Haiyan et al. [75] reported the observation of SF induced twinning and HCP transformation (

Figure 3).

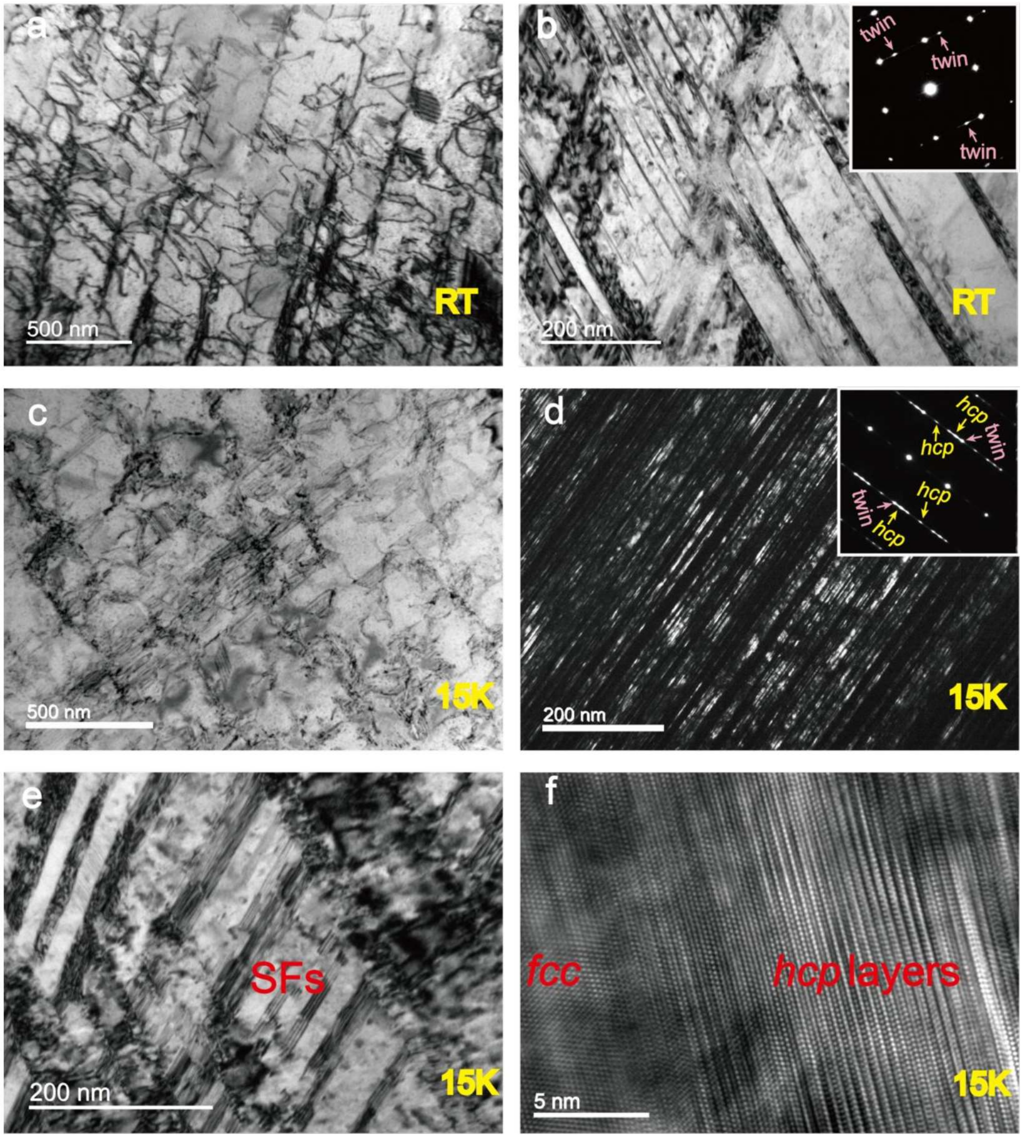

Figure 3. Bight-field (BF) and dark-field (DF) TEM images of NiCoCr MEA samples subjected to tension up to fracture at RT and 15 K. a) Dislocations and numerous stacking faults, RT sample. b) Deformation twinning and selected-area diffraction (SAD) pattern for further evidence (inset). c) Dislocations and SFs, 15 K sample. d) DF image showing HCP phase with further evidence by SAD pattern (inset). HCP lamellae and SFs. f) HRTEM image of adjacent regions of FCC and HCP [75].

In another study, Sezer et al. [84] investigated the work hardening behavior of single crystalline $Fe_{40}Mn_{40}Co_{10}Cr_{10}$ HEA. Their TEM observations show several stacking faults, as can be seen in

Figure 4 Furthermore, an interaction between SFs and twinning was also detected (

Figure 4b), declaring how SFs play an important the role in effecting the mechanical behavior and deformation mechanisms exhibited by the material.

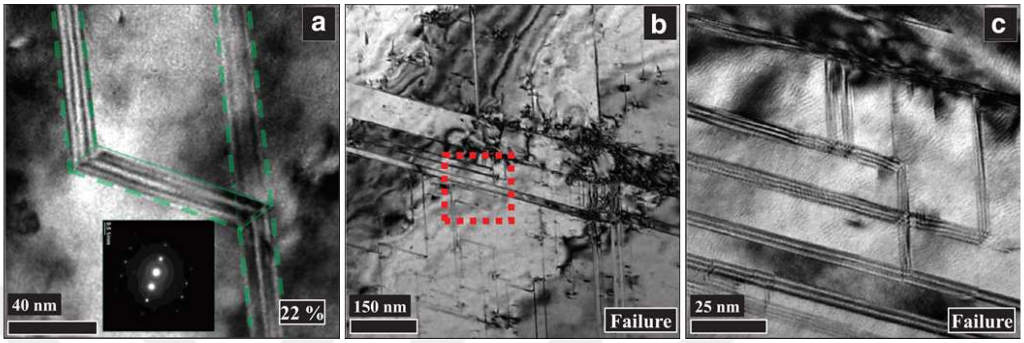

Figure 4. TEM images of $Fe_{40}Mn_{40}Co_{10}Cr_{10}$ HEA deformed up to failure. a) SF parallelepipeds. b) a SF-twinning interaction. c) zoom-in of the dotted red squared area in b) [84].

1.2.2. Short-range Ordering in Medium and High Entropy Alloys

Short-range ordering, defined as the correlation of occupied local lattice sites, is one significant factor that has an effect on dislocation plasticity in MPEAs [85–88]. The presence and degree of symmetry or correlation in a system is designated by order and disorder. A random solute solution state can be achieved at high temperatures, whereas preserving it requires fast cooling rate. However, the presence of disorder at thermodynamic equilibrium dismantles the state of random solute solution [89]. In contrast, the differentiation of the odds that specific sublattice positions will be occupied by specific atoms is known as long-range order

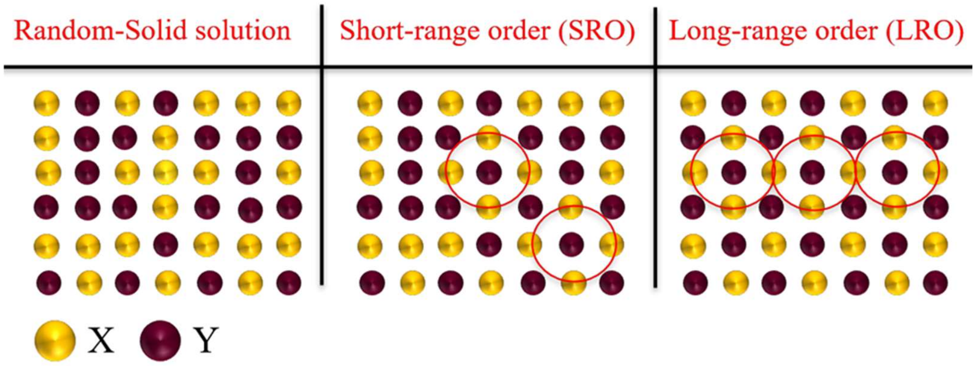

Figure 5. Schematic illustration of random solid solution, short-order and long-range order in a binary system [74].

Given their chemical complexity, HEAs strongly tend to exhibit SRO [90]. However, due to the complexity in its local atomic environment, the increasing number of components makes SRO formation more difficult [91,92].

The presence of SRO prevents cross-slip and can promote dislocation pile ups in FCC solid solutions [85–88]. This has encouraged researchers to prove SRO existence and its influence on mechanical response of M/HEAs [16,20,22]. However, there are still conflicts regarding how SRO affects the deformation behavior and mechanical response of M/HEAs, mainly NiCoCr MEA. Zhang et al. have reported that, despite having a very low stacking fault energy (8.18± 1.43 mJ/m2), as-quenched samples of polycrystalline NiCoCr do not experience planar slip due to lack of SRO, while the aged samples exhibit planar dislocations even though they possess a higher degree of SRO, no second phase precipitates and almost triple the amount of SFE of the as-quenched samples [22]. However, previous studies [3,64,93] strongly disagree with these findings, reporting pronounced planar slip in as-quenched samples of NiCoCr with a medium SFE (22 ± 5 mJ/m2) exhibiting pronounced planar dislocations. Moreover, the claim that higher SRO degree samples of NiCoCr exhibit higher yield strength and hardness contradict with Yin et al. results, concluding that there was no appreciable SRO degree dependence of yield strength and hardness in NiCoCr [94]. It is known that dislocation structure in FCC materials is strongly dependent on the grain orientation, SFE, SRO and precipitates [85,95]. Therefore, the disparities in findings might stem from, rather than SRO, either presence of precipitates or the tests being conducted in different crystallographic orientations, resulting in higher yield strength and hardness. Thus, a more precise investigation of the effect of SRO on the mechanical behavior of M/HEAs needs to be established to resolve the conflict and reveal the underlying secrets behind those outstanding mechanical properties.

1.2.2.1. SRO Characterization

As precedingly mentioned, SRO has a strong effect on the mechanical properties of HEAs. Thus, precise characterization and description of SROs in these complex alloys become essential for a further comprehension of the SRO-properties relationship and a better design of HEAs with higher potential. In this regard, there are two aspects of SRO characterization, namely quantitative description and direct observation [96]. 3D atom probe tomography (3D-APT) has shown a potential for SRO characterization. A recent study conducted by Maiti et al. [97] showed that reconstruction of lattice-based distribution of atoms can be achieved by combining the APT data, as shown in Figure 6a. However, this approach still struggles to handle the complicated field evaporation for the SROs with subtle chemical differences from the matrix [90]. Direct observation of SRO is not any less challenging, as appropriate scattering contrast (the deviation in atomic size, mass, etc.) between atoms is needed to define particular atomic pairs. Additionally, SRO presence makes this even more complicated. To overcome this, techniques can be utilized such as high-precision probing such as the abnormal X-ray diffraction, where altering the input beam energy around the elements' absorption edges (such as Cr, Fe, and Ni) helps distinguishing between the scattering contributions of various constituents [91]. Techniques with enhanced diffraction contrast, such as energy-filtered diffraction pattern, are also practical in directly observe scattering signals of SRO, as shown in Figure 6b [22,98]. However, this streaking is not necessarily an SRO indicator, as they are more commonly attributed to planar defects, e.g., stacking faults [99]. Furthermore, this claim lacks theoretical support verifying that these streaks are distinct identification of SRO domains with nanoscale diameter.

Recently, a couple of studies claimed that streaks connecting Bragg diffractions can be an indicator of medium-range ordering, as they are designated by a directional diffuse intensity, which can overlap with the diffuse intensity caused by soft vibrational modes [22,100,101].

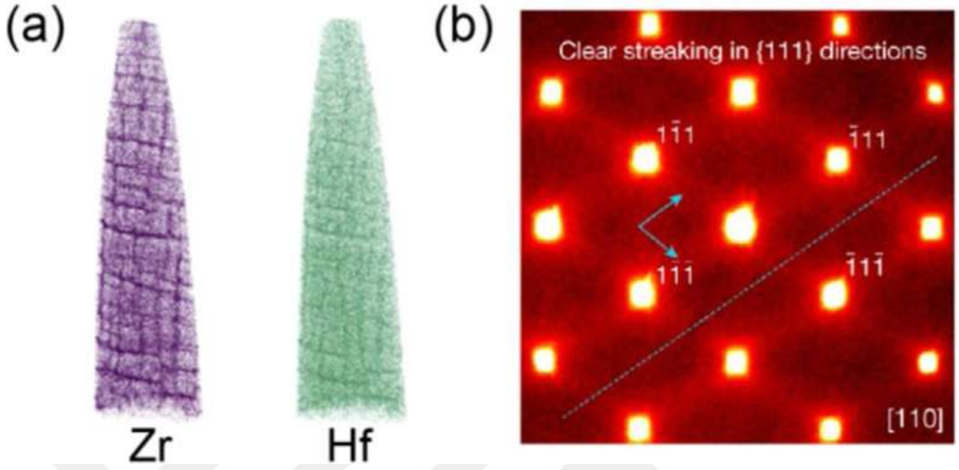

Figure 6. Experimental characterization of SRO by a) APT, conducted on an annealed TaNbHfZr HEA, b) energy-filtered diffraction pattern, conducted on NiCoCr MEA. The APT measurements indicate SROs enriched by Zr/Hf [97]. The distinct streaking stems from SRO domains' diffuse scattering signals [22].

Liu et al. [102] reported an observation of SRO in $Fe_{50}Mn_{30}Co_{10}Cr_{10}$ HEA, utilizing high-angle annular dark-field (HAADF) in a scanning transmission electron microscopy (STEM), along with the corresponding Fast Fourier Transform (FFT), as shown in

Figure 7 They claim that the extra diffusions (one circled in yellow) are indicator of SRO presence. Furthermore, they employed energy dispersive X-ray spectroscopy (EDS) mapping and got a map from the HAADF image, as shown in

Figure 8 It can be clearly seen from the zoomed-in maps that there is an Fe concentration on every other atomic plane.

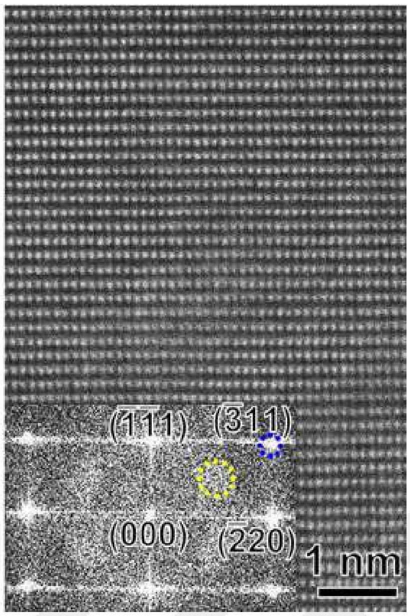

Figure 7. STEM-HAADF image with the [112] zone axis, FFT pattern inset. Note that there are extra diffusions at $\frac{1}{2}\{\bar{3}11\}$, as well as the sharp Bragg spots from FCC diffraction [102].

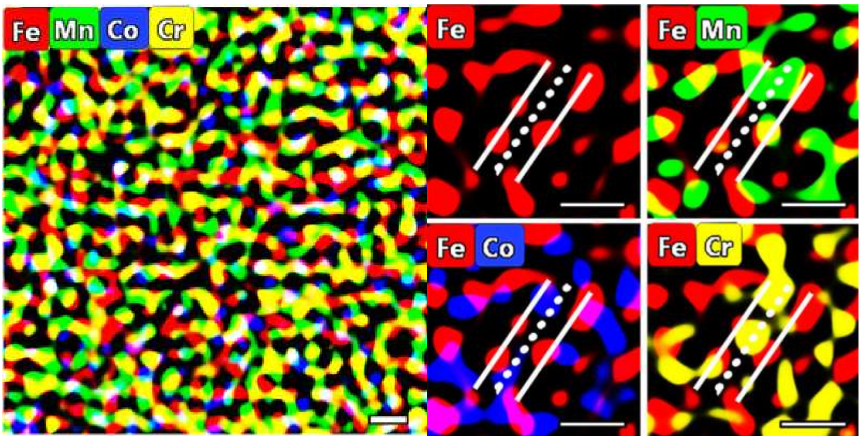

Figure 8. EDS mapping from the HAADF image in

Figure 7 with zoomed-in maps. White lines mark the intersection between $(\bar{3}11)$ and (111) planes [102].

SRO was further identified in NiCoCr MEA single crystals using polar synchrotron transmission x-ray diffraction spectra (

Figure 9) [100]. Diffuse diffraction spots can be observed in both water-quenched (

Figure 9a) and 48h-aged (

Figure 9b) samples. Although the diffusion of the spots remains the same, there is a clear increase in the intensity in the 48h-aged sample as compared to the WQ sample. This intensity increase indicates a transition state between short-range ordering and long-range ordering, i.e. medium range ordering (MRO), which is presumed to be an extension/growth of SRO [100,103].

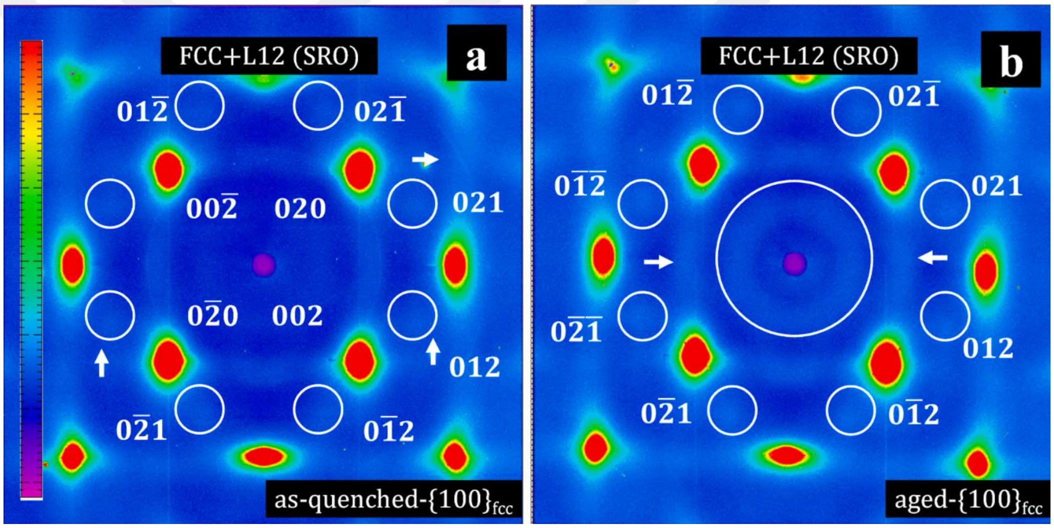

Figure 9. Investigation of SRO in NiCoCr MEA single crystals in the [001] zone axis using polar synchrotron transmission x-ray diffraction spectra [100]. a) WQ, b) 48h-aged samples. The extra reflections indicating SRO can be seen in both samples (white circles).

1.2.2.2. Tuning The Degree of SRO

Thermally activated SRO formation techniques, e.g., aging, have been widely studied in the literature [100,104–107]. On the other hand, tailoring the degree of SRO is also possible via subjecting the material to mechanical load. This mechanically-driven SRO was proposed by Seol et al. [108], where they apply a tensile load on polycrystalline $Fe_{40}Mn_{40}Cr_{10}Co_{10}$ HEA at 77 K. Moreover, they reported that the degree of SRO can be further tuned by changing the loading rates. In terms of characteristics and observations, the resulting mechanically-derived SRO (MSRO) is no different from the thermally activated SRO, as they both display diffuse scattering in the SAD pattern (Figure 10). Furthermore, they both double the {311} interplanar spacing compared to that one in the FCC lattice. However, the nucleation of MSROs is attributed to edge dislocations and SFs within atomic-packing-displacement-driven slip bands. Moreover, the majority of MSROs have a consistent distribution along the slip bands in each particular grain of the distorted material. This provides a clear distinction between the formation mechanism of the precedingly existing SROs and the MSROs, despite both causing the same diffuse scattering indicators at $^1/_2\,\{311\}$ locations in the SAD pattern [108].

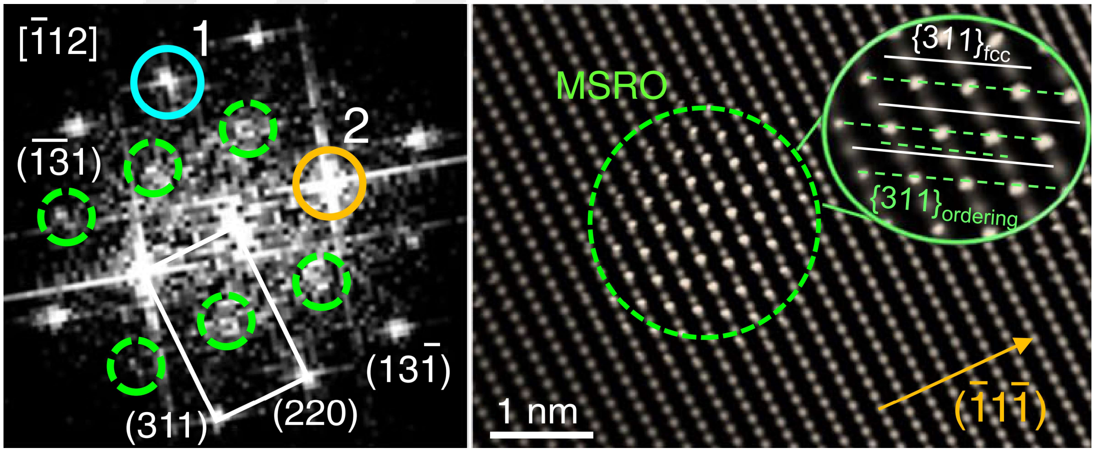

Figure 10. STEM-FFT pattern showing MSRO (left). Inverse FFT pattern created by superimposing a single MSRO domain with FCC lattice fringes (right) [108].

1.2.2.3. SRO-Mechanical Properties Relationship

SRO is believed to have a substantial effect on the mechanical properties of MPEAs. In fact, several studies have already approached enhancing the mechanical properties of MPEAs via tuning the degree of SRO, including SFEs, strain hardening, hardness and yield strengths [16,22,96,100,104,105,109,110].

In their study, Sezer et al. [100] investigated the SRO-mechanical property relationship, and claimed that the SRO influence on the mechanical properties was strongly orientation-dependent. Furthermore, they claimed that a rarely observed simultaneous TWIP and TRIP was triggered by SRO.

Figure 11 shows the mechanical responses of [111]-, [110]- and [001]-oriented WQ and 48h-aged samples of single crystalline NiCoCr MEA, subjected to tension at 300 K. Overall, SRO had a minor effect on the yield strength, while it strongly enhanced the strain-to-failure and the ultimate tensile strengths, clearly seen in the [111]- and [110]-oriented aged samples. The mechanical responses of [001]-oriented WQ and aged samples, however, were nearly the same. This indicates a strong orientation dependence of the SRO effect on the mechanical behavior of NiCoCr MEA.

In this context, Zhang et al. [22] were able to achieve an appreciable increase in the yield strength of polycrystalline NiCoCr MEA, after aging at 1000 °C for 120 h. According to the authors, this increase in the yield strength affirms the effect of SRO on the mechanical properties of NiCoCr MEA.

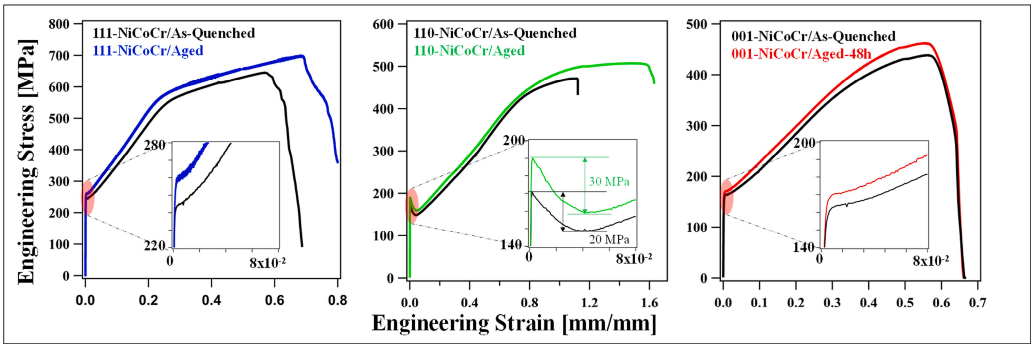

Figure 11. Tensile test results of [111]-, [110]- and [001]-oriented WQ and 48h-aged samples of single crystalline NiCoCr MEA, at 300 K [100].

Chen et al. [110] conducted on polycrystalline VNiCo MEA reported dislocation pile-up around SRO domains, indicating a strong relationship between dislocation motion and the existence and degree of SRO. According to the strain maps generated using geometrical phase analysis (

Figure 12), prior to tensile loading, yellow areas designate elastic compressive strains produced by SRO domains, as V-enriched planes alternate with V-depleted ones. The post-deformation strain map, however, shows multiple neighboring red and blue regions on top of the yellow regions (SRO domains). Accordingly, Chen et al. suggest that this local strain might stem from a pairing of SRO and dislocations caused by an increase in the force required for a dislocation to overcome the SRO domains.

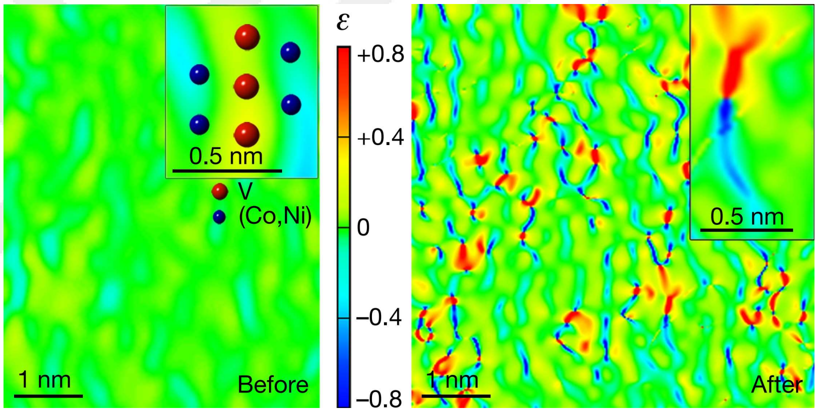

Figure 12. Local strain maps generated using geometrical phase analysis (GPA) in VNiCo MEA, before (left) and after (right) deformation. The inset on the left illustrates the alternating planes in the SRO. A close-up view of a contrasting local strain can be seen in the inset on the right [110].

1.2.3. Strain Hardening Behavior of Medium/High Entropy Alloys

Besides the unique mechanical properties, M/HEAs exhibit exceptional strain hardening behavior, which is, in some cases, comparable to the so-called TWIP Steels. The strain hardening of low SFE FCC alloys is divided into four distinct stages. Stage I is mostly governed by dislocation propagation, and it is similar to stage III of high SFE FCC alloys, in which the ongoing decrease of strain hardening is prevalent [13,14,111]. Asgari et al. [13] claimed that twinning does not occur in stage I. However, overlapping stacking faults take place in this stage, indicating dislocation interactions which form sites for twin nucleation. The major twinning stage, or stage II, is distinguished by an increasing strain hardening. It begins with the formation of primary twins in the grains with favorable orientation. The strain hardening rate increases during this stage and then essentially stays constant. The onset of stage II is usually around true strains of 0.03-0.04, indicating that dislocation-dislocation interactions and the activity of dislocation slip take place before twinning [111]. Despite the dramatic rise in strain hardening at the onset of stage II in

Figure 13, it is of importance to mention that this is not always the case. However, there are some disagreements upon stage II being totally attributed to the onset of deformation twinning, rather, some link the onset of this stage to a twinning rate increase [1], or to a secondary twinning system being activated [48,49]. The maximum strain hardening rate is seen at the stage II to stage III transition. During stage III, strain hardening rate progressively decreases due to descension in primary twin formation rate. As deformation twins are forming, grain size decreases, and thus further twin formation will require higher stresses [50]. Kalidindi et al. [13,14] suggest that the gradual decrease of strain hardening in stage III comes to an end owing to the initiation of twinning on secondary twin systems. These four stages are the most agreed upon by researchers. However, there are some studies that suggest more than four stages. Proposing a fifth stage, Barbier et al. [48,51] claim that the continuously diminishing strain hardening rate occurs during this stage due to the substantial increase of twin volume fraction. Yet, this finding seems to have contradiction with the well-established saturation of deformation twinning.

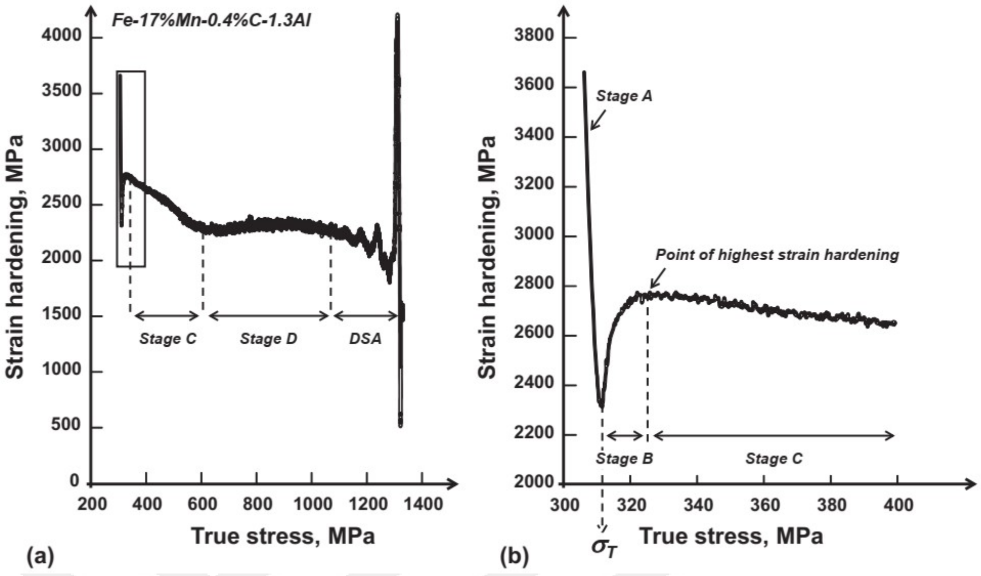

Figure 13. a) Illustration of four strain hardening stages of Fe-17%Mn-0.4%C-1.3%Al TWIP steel. b) Enlargement of the area defined indicated in a). σ_T is the twinning stress. The strain hardening rate peaks at the transition from stage II to stage III [111].

1.2.4. Interstitial Effect on Mechanical Properties of M/HEAs

HEAs differ from conventional alloys in many aspects, substantially the in solute solvent concept, as it is absent in HEAs. In traditional alloys, to form an interstitial solid solution by filling lattice gaps with solute atoms, the difference in the atomic radii must be larger than 41% [112]. Non-metallic interstitial elements such as carbon, boron, nitrogen and oxygen, which are known to possess very small atomic radii (less than 0.1 nm), still produce distortion when entering the lattice gap, owing to the fact that the gap is yet smaller than these atomic radii. Depending on the degree of lattice distortion caused by interstitial doping, the alloy properties can be significantly affected [113]. These non-metallic elements are often doped into conventional alloys as gap atoms, which can either reinforce the alloy in a solid solution or play a second phase strengthening role by building stable carbon compounds with the alloying elements. For example, the doping of carbon or nitrogen doped steels exhibit both solid solution strengthening and second phase precipitation, altering the performance of the material [114]. Lattice distortion, however, plays a critical role in nitrogen- and oxygen-doped titanium alloys, impeding dislocation movement, and thus enhancing the mechanical properties [115]. This method can be extended to HEAs, further enhancing their properties and providing a much broader field of choices in terms of interstitials-chemical composition combination. However, there are certain cautions need to be taken when doping HEAs with interstitial atoms. First, if the HEA is overdoped with interstitials (the amount of interstitials is beyond the solubility limit), undesired ceramic phases will form, acting as crack propagation areas due to their brittleness, deteriorating the mechanical properties of the alloy [116]. Second, despite the advantageous attribute of interstitials to mechanical properties, it is still possible to have segregations at internal stress concentrated areas, such as grain boundaries and crack tips, which leads to concentration of local stress, thus acting as crack nucleation areas and resulting in early failure of the alloy [116].

1.2.4.1. Effects of C Doping

Having an atomic number of 6 and radius of 0.8 nm, C is considered the most widely used doping element in alloy design, mainly for two reasons. First, C has a high solubility in austenite, which facilitates the formation of a solid solution structure, enhancing the mechanical properties of the alloy [117,118]. Wang et al. [119] were able to achieve a ~120% increase in yield strength of $Fe_{40.4}Mn_{34.8}Ni_{11.3}Al_{7.5}Cr_6$ HEA via C doping. Second, C doping can also result in carbide structure formation, which is known to enhance yield strength [120], hardness [121] and wear resistance [122]. C doping also governs and affects the microstructure phase in HEAs, as Bai Li et al. [123] doped 5% C into $Fe_{40}Mn_{30}Ni_{10}Cr_{10}Al_{10}$ HEA, and their results indicate that the microstructure went from being a dual phase (BCC and FCC) to a single FCC phase. Guo et al. [120] studied the effects of C interstitials on equiatomic FeCoCrNiMn HEA, manufactured by arc-melt method in a water-cooled copper crucible in Argon atmosphere. Three different variants of the alloy were prepared, with the C content being 0 at%, 0.5 at% and 1.0 at%. From the XRD analysis (

Figure 14), besides the FCC peaks, delicate diffraction peaks were detected in the C0.5 and C1.0 samples, designating $M_{23}C_6$ carbides at (422) and (511) planes. This indicates that $M_{23}C_6$ carbides were formed during annealing after cold rolling.

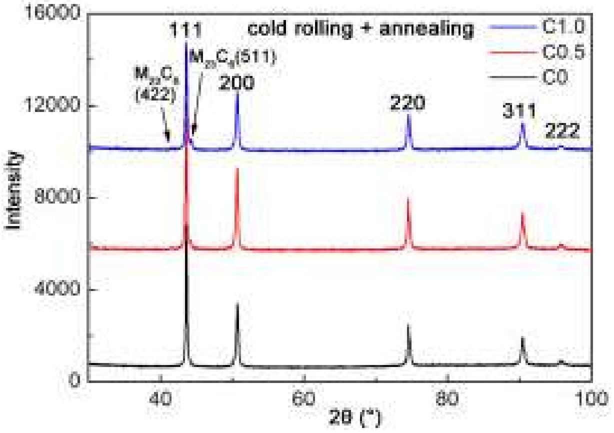

Figure 14. XRD analysis of FeCoCrNiMn HEA with varying C concentrations.

However, one of the challenges encountered is the determination of the right amount of interstitial C to be doped. Chen et al. [124] conducted a study on the design and effect of C doping on $(Fe_{40}Mn_{40}Ni_{10}Cr_{10})_{100-x}C_x$ HEA. What they found out was that doping 3.3% C resulted in the best combination of mechanical properties. This addition of C reduced the SFE of the alloy, promoting deformation twinning and thus TWIP effect, which can be clearly seen in the EBSD characterization (

Figure 15).

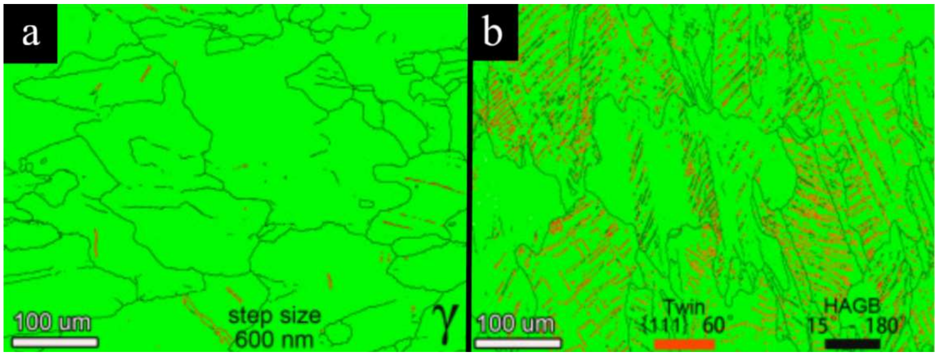

Figure 15. EBSD maps showing the post-fracture microstructure of a) C0 and b) C3.3 samples of the HEA [124].

1.2.4.2. Effects of N Doping

Among all interstitial elements, N is the most efficient in terms of stabilizing FCC phase in the matrix so far [125]. Based on previous studies [125–129], N doping can improve the mechanical properties of HEAs, including yield strength, ultimate tensile strength and strain hardening behavior of the material. Moreover, N doping was proven to contribute in grain refinement, further enhancing the mechanical performance of the material [130]. Lee et al. [131] compared nitrogen doped FeMnCoCr HEA to its nitrogen-free counterpart, and found that when even a small amount of N enters the matrix, the forming Ng phase stabilized the FCC phase by impeding the deformation and thermally induced phase transformation, which is further proven by the EBSD images (

Figure 16). Furthermore, N doping also had an effect on the yield strength of the alloy, as it increased from 472 MPa to 503 MPa, as well as ductility (from 23% to 48%), after 1.0% N addition. The yield strength improved with further addition of N, as the alloy reached a yield strength of 602 MPa. The work hardening rate of the alloy barely changes with the addition of 1.0% N. However, with the increase of N content, the work hardening rate is dramatically enhanced.

Han et al. [132] introduced N into CoCrFeMnNi HEA, and examined its effect on the mechanical properties of the alloy. From their findings, it was concluded that N doping substantially enhanced the strength of the alloy, while the change in ductility was negligible.

Additionally, other studies reported that N doping shows a lot of promise for material surface engineering [133]. N-containing VAlTiCrMo HEA coating was examined by Chen et al. [134]. The outcomes demonstrated that N changed the coating's phase structure from BCC to FCC and enhanced its hardness and elastic modulus. By using reactive sputtering, Cheng et al. [135] created HEA (AlCrMoTaTiZrN) films with varying N concentrations and attained an ultra-high hardness of 40.2 GPa.

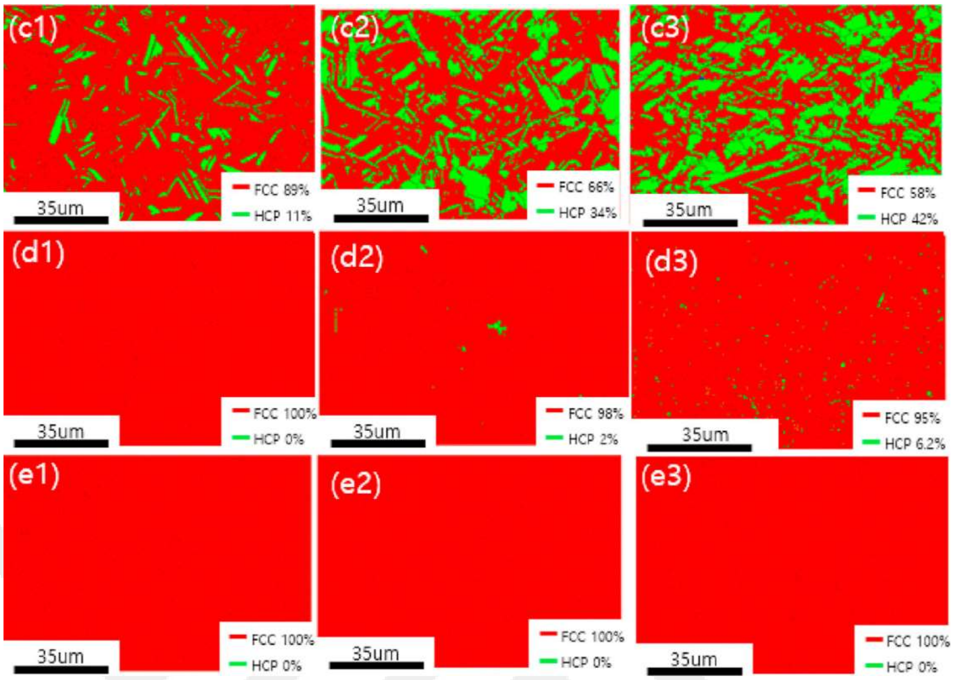

Figure 16. EBSD maps showing phase distribution of $Fe_{50}Mn_{25}Cr_{15}Co_{10}$, annealed (c1), strained to 10% (c2) and 20% (c3); $Fe_{50}Mn_{25}Cr_{15}Co_{10}N_{1.0}$, annealed (d1), strained to 10% (d2) and 20% (d3); (e1-e3) EBSD phase map of $Fe_{50}Mn_{25}Cr_{15}Co_{10}N_{1.6}$, annealed (e1), strained to 10% (e2) and 20% (e3) [131].

1.2.4.3. Effects of O Doping

Oxygen doping usually forms impurities undesired in metals, such as oxide particles [113]. Despite its positive effect on strength, O doping increases brittleness of the material. Therefore, it is crucial to avoid the brittle phases during metal production. Nevertheless, recent studies have found that O doping can form high solubility interstitial solid solutions in HEAs made up of transition metals, including Ti, Zr, Hf [136], V [137], Nb [138], Ta [139]. For Ti alloy [140], O doping produces interstitial solid solution in Ti, increasing the lattice distortion, impeding dislocation motion, therefore increasing the strength [141,142]. Chen et al. [143] conducted a research on $ZrTIHfNb_{0.5}Ta_{0.5}O_x$ HEA. Specimens of the alloy were conducted to compressive load at (25˚C, 700˚C, 800˚C). They conclude that low O containing alloy (0.05, 0.1) exhibits good ductility at RT (>50%), and the yield strengths are 955 MPa and 1097 Mpa, respectively. With the increase of O content (0.2), the yield strength is slightly enhanced (1393 Mpa) at the expense of ductility (8.2%). O doping was also found to inhibit the martensitic transformation in $Ti_{23}Nb_{0.7}Ta_2Zr$ [144]. Lei et al. [145] reported that doping 2% O into TiZrHfNb HEA resulted in a 50% increase in yield strength, as well as a 100% increase in ductility, breaking the so-called strength-ductility trade-off [146]. Interestingly, O atoms form a new state different from traditional interstitials, called “ordered oxygen complexes” (OOCs) [147].

1.2.4.4. Effects of B Doping

Boron is usually doped into Ni-based and Ti-based alloys, and has increasingly been proposed for use in HEA systems [148,149]. Unlike other interstitial elements, B has a lower formation enthalpy, facilitating the formation of hard second phases [150]. Hou et al. [151] doped different amounts of B into AlFeCoNi HEA. Their concluded that increasing the amount of B resulted in higher yield strengths. Moreover, B promotes grain refinement, thus enhancing the mechanical properties of the alloy [152].

1.2.5. Plastic Deformation in Single Crystals:

Single crystalline M/HEAs, just like any other single crystal, obey Schmid’s Law, which states that shearing on a slip system can be initiated only if its corresponding resolved shear stressreaches a critical value, called the critical resolved shear stress.

The critical resolved shear stress (τ_{cr}) can be calculated from the formula:

$$\tau_{cr} = \sigma_s \cos \lambda \sin Ø$$

Where σ_ε is the applied tensile stress, λ is the angle between the loading direction and the normal to slip plane, Ø is the angle between the loading direction and the slip direction, which is {111} for fcc crystal structure. The product $\cos \lambda \sin Ø$ is called the Schmid factor, m.

The Schmid factors for fcc crystal structure, for slip and twinning for both tension and compression, as well as the number of the most favorable slip/twinning systems that have the sameSchmid factor, are listed in Table 2.

Table 2. Schmid factors for slip and twinning in [001], [111] and [123] directions for tension and compression [46].

Axis	**Tensile Schmid Factors**		**Compressive Schmid Factors**	
	Slip	**Twin**	**Slip**	**Twin**
[001]	0.41 8 Sys.	0.23 8 Sys.	0.41 8 Sys.	0.47 4 Sys.
[111]	0.28 6 Sys.	0.31 3 Sys.	0.28 6 Sys.	0.16 6 Sys.
[123]	0.46 1 Sys.	0.47 1 Sys.	0.46 1 Sys.	0.34 1 Sys.

We see that the number of favored systems with equivalent Schmid factors varies from 1 to 8. Table 2 shows that both the loading direction and the crystallographic orientation have an effect on the resulting favored deformation mechanism. Notice that loading direction doesn't havean effect on slip Schmid factors, whereas it crucially influences on twinning Schmid factors.

1.2.6. Manufacturing Techniques of Single Crystals

1.2.6.1. Zone Melting

Zone melting is a method employed in the production of single crystals, in which a molten zone of a crystal is passed along, melting the impurities at its edge, resulting in a pure solid material behind. By concentrating the impurities in the melt, it is possible to transfer them to one side of the ingot. The regulated motion of the molten zone helps purifying the material and facilitates the formation of a single crystal [153]. This method was first used commercially in germanium, achieving an impurity of one atom per ten billion, yet it can be applied to nearly any combination of solute and solvent where there's a significant difference in concentration between the solid and liquid phases at equilibrium [154].

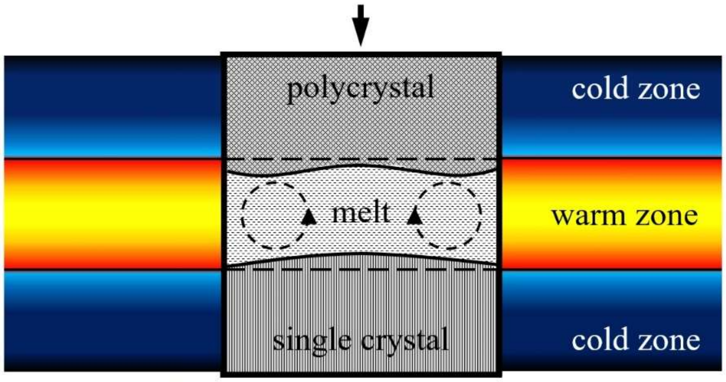

Figure 17. Zone melting. [155].

Experimental Setup:

Chamber: The process typically takes place in a controlled atmosphere, often in a vacuum or inert gas environment to prevent contamination from the surroundings.

Heating Element: A localized heating element is employed to create a narrow molten zone along the length of the crystal rod.

Crystal Rod: The material to be purified is usually in the form of a rod or ingot, placed horizontally within the chamber.

Temperature Control: Precise temperature control is crucial to maintain the molten zone at a temperature slightly above the melting point of the material [156].

Applications:

Semiconductor Industry: Zone melting is extensively used in the semiconductor industry for the production of high-purity silicon crystals used in integrated circuits and other electronic devices [157]. The exceptional purity levels achieved through zone melting are crucial for ensuring the performance and reliability of semiconductor devices.

Materials Science: Beyond semiconductors, zone melting is employed in the purification and growth of various crystalline materials used in optics, photovoltaics, and other advanced technologies where purity is paramount [156,157].

1.2.6.2. Directional Solidification Methods

Heat flow direction and cooling rate directly affects the grain formation and orientation. In general, grain direction is parallel to the heat flow direction. Directional solidification method is based on the movement of the mold from heating zone to cooling zone at a certain speed. This method is suitable for industrial scale manufacturing and widely used in manufacturing of nickel-based superalloy gas turbine blades [158].

1.2.6.3. Power Down Method

This method is based on the progressive reduction of the temperature in the furnace. Although it does not require the displacement of the mold with molten metal from the heating furnace, cooling water at the bottom of cooling chill plate for cooling operation is needed [158].

Preparation:

First, the mold is placed in the heating furnace on the copper chill plate. Then, the chamber is vacuumed. Afterwards, the mold is heated to the desired temperature. Meanwhile, metal ingot is melted using induction heating. After the mold reaches the temperature throughout its whole volume the molten metal is filled into the mold. After the pouring process is done, the lid is closed and the lower heater element is switched off [159].

Cooling:

The liquid metal in contact with the chill plate begins the process of solidification. The upper heating element is kept on at this point. This allows for columnar grain growth parallel to the heat flow direction. After all liquid metal is cooled down, the directional solidification process is finished [160].

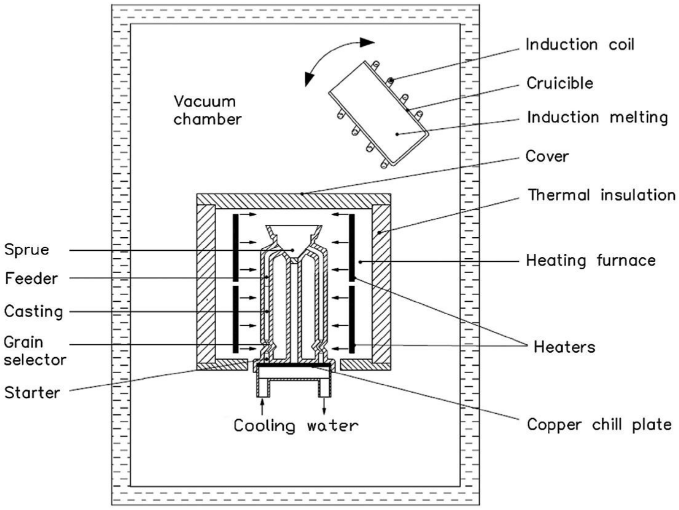

Figure 18. Power down method schematic [159]

1.2.6.4. Bridgman-Stockbarger Method

The Bridgman-Stockbarger method is a technique used in materials science and crystal growth to produce single crystals of various materials, particularly semiconductors [161]. It was developed by Percy Williams Bridgman and John C. Stockbarger in the early to mid-20th century. The process begins with placing the material to be crystallized in a refractory crucible capable of withstanding high temperatures [162]. Afterwards, the process will carry on as follows.

Heating:

The crucible is subjected to high temperatures in a furnace until the material melts and forms a molten phase [162]. In order to make sure the crystal grows in a specific direction, a temperature gradient must be established within the crucible [163].

Seed Crystal Introduction:

A seed crystal, usually of the same material as the one being grown, is introduced into the molten phase at the higher temperature end of the crucible [164].

Controlled Cooling and Crystal Growth:

As the temperature decreases, the molten material begins to solidify around the seed crystal, forming a single crystal with atoms arranging themselves in a crystalline structure [164].

Pulling Process (Optional):

In some variants of the Bridgman method, the crucible may be slowly pulled upwards or downwards during the cooling process to further control the growth rate and quality of the crystal [165].

Harvesting and Processing:

Once the crystal growth is complete, the single crystal is carefully harvested from the crucible and may undergo additional processing steps such as cutting, polishing, and doping to tailor its properties for specific applications [162].

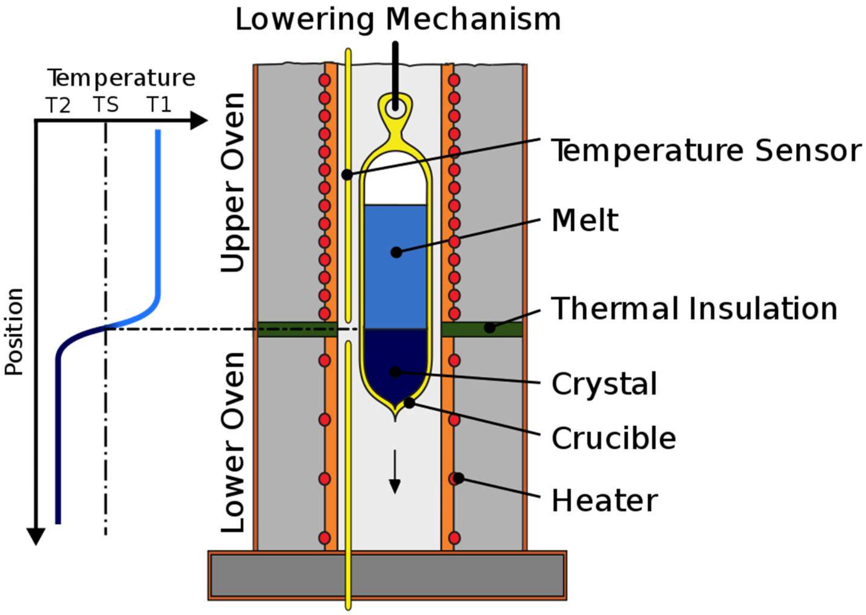

Figure 19. Bridgman-Stockbarger Method [161].

1.2.6.5. Liquid Metal Cooling (LMC) Method

This method is very similar to Bridgman-Stockbarger method. While chill ring is used in Bridgman method, this method uses a cooling bath filled with liquid metal instead (usually aluminum and tin, due to their low melting points, high thermal conductivity and cost efficiency) [158].

The mold is heated in a furnace using radiant heaters, then it is moved with a specific speed to the coolant bath. The coolant bath is continuously stirred and kept at a constant temperature during the cooling process. Finally, the solidified metal is obtained [160].

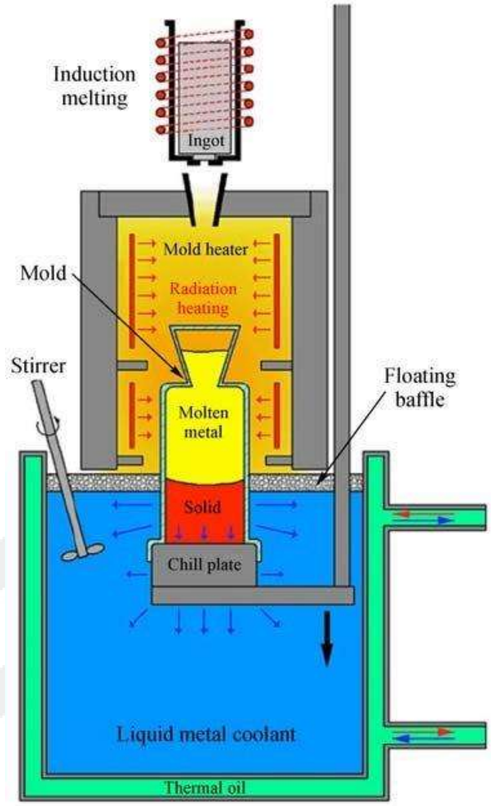

Figure 20. LMC Method Schematic [166].

1.2.6.6. Chemical Vapor Deposition (CVD)

Chemical Vapor Deposition (CVD) crystal growth method is a technique used to grow single-crystal materials through the chemical reaction of gaseous precursors on a substrate [167]. This method allows for the precise control of crystal growth parameters, resulting in high-quality crystals with tailored properties. It involves the decomposition or reaction of gaseous precursor molecules at the surface of a heated substrate, resulting in the deposition of crystalline material [168]. Selecting appropriate precursor materials is crucial for CVD crystal growth. These precursors should be volatile compounds that can undergo controlled decomposition or reaction to form the desired crystal structure [167]. The CVD crystal growth process typically occurs within a reaction chamber maintained at controlled temperature and pressure conditions. Heating the substrate to elevated temperatures facilitates the decomposition or reaction of precursor gases [168].

Prior to crystal growth, the substrate surface is often cleaned and prepared to promote nucleation and adhesion of the deposited material [169]. Then, the precursor gases are introduced into the reaction chamber, where they come into contact with the heated substrate surface. These precursors may be introduced separately or as a mixture, depending on the desired crystal composition and properties [170].

Upon reaching the heated substrate surface, the precursor molecules undergo chemical reactions such as decomposition, pyrolysis, or reduction, leading to the formation of solid-phase crystalline material. This material then grows epitaxially on the substrate, following the crystal lattice orientation of the substrate [171]. Various parameters such as temperature, pressure, precursor flow rates, and substrate composition are carefully controlled to achieve the desired crystal growth characteristics, including crystal size, orientation, and quality.

The growth mechanisms during CVD crystal growth can vary depending on factors such as precursor chemistry, substrate surface properties, and reaction conditions. Common mechanisms include surface adsorption, surface diffusion, and bulk diffusion [168].

1.2.6.7. The Czochralski Method

In this method, the melt is kept at a temperature slightly above its freezing point. Then, a seed crystal rigidly fixed to a rotating tube is lowered into the surface of the melt. The temperature of the melt is reduced until the molten material begins to freeze onto the seed. Afterwards, the rod is pulled while rotating and more material solidifies onto the seed crystal. Rotating the rod produces stirring effect, promoting homogenization of the melt [172].

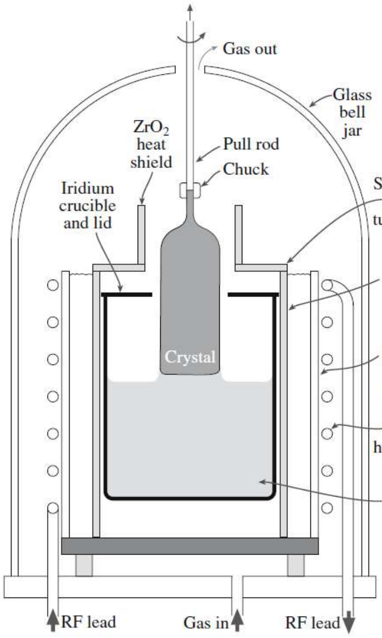

Figure 21. The Czochralski method schematic [173].

1.2.7. Polycrystalline M/HEAs

Apart from single crystals, polycrystalline M/HEAs are also of much interest due to their superior performance in most engineering applications, as well as the outstanding mechanical properties they possess (e.g. yield strength, toughness and strain hardening rate) when compared to their SC counterparts. Most importantly, polycrystalline materials, unlike SCs, exhibit an isotropic (independent of orientation) mechanical behavior in most cases, which explains their preference over SCs in most applications. For polycrystalline materials, the main focus will be ongrain refinement, as it is widely known for its success in crucially alter the mechanical propertiesof metallic alloys. Severe plastic deformation (SPD) is an effective mechanism that has been wildly employed to increase the strength at the expense of ductility to a high extent [174–179], which can reach very high values of yield strength, e.g., a yield strength of (~1.2 GPa) in ECAP processed NiCoCr MEA [179]. The reduced grain size and increased dislocation density achieved through SPD contribute to an enhancement of the yield strength. One of the most efficient grain refinementmethods is deformation twinning, as dislocation motion is restricted at twin boundaries, leading tothe so-called Hall-Petch effect [84]. TRIP is also a desired deformation mechanism in fcc crystals,since it leads to toughening at ambient and low temperatures. A distinction between these two mechanisms is that TWIP can only take place at cryogenic temperatures [48], whereas TRIP is most often observed at both ambient and low temperatures [1].

High pressure torsion (HPT), and equal channel angular pressing (ECAP), are one of the most well-known SPD methods capable of producing ultra-fine grained (UFG) structures. However, ECAP is still more efficient in processing relatively large samples, where all dimensionscan exceed a centimeter, and it provides a relatively uniform microstructure. Moreover, the unchanging cross section allows for multiple repetitions of the process, if it is within the material processing capacity, until the desired microstructure and deformation levels are achieved. The impacts of grain size reduction via various thermomechanical techniques on the mechanical properties of HEAs have been studied under uniaxial loading [174–178,180–182]. Although HPT has shown success in increasing the strength and hardening of CoCrFeMnNi HEA [181,182], its major drawback is the low ductility level of the samples [181,182]. To resolve this, annealing is usually applied, leading to grain growth, and phase decomposition, reducing the strength and producing a more complex microstructure[181,182]. Many HEAs have been HPT processed, however, an increase in strength was achieved at the expense of ductility. A more favorable strength-ductility combination was achieved in CoCrFeMnNi through the precedingly mentionedECAP method, demonstrated by Shahmir et al. [178].

1.2.8. Non-monotonic Loading and Fatigue Lives of M/HEAs

In most engineering applications, alloys are usually subjected to cyclic loading. Furthermore, mechanical behavior and microstructural evolution of conventional alloys can differextensively based on loading conditions, specifically in under cyclic loading [183,184]. Hence, studies focusing on the cyclic response of HEAs are essential in order to reveal their deformationbehavior under cyclic loading, estimate their fatigue lives, and develop HEAs with higher fatigue resistances. While failure can still occur at relatively low stresses, many applications have high loads and, hence, materials exhibit at least minor yielding in each cycle, ultimately leading to shortfatigue lives [185,186]. Despite having many researches conducted on the low-cycle fatigue

(LCF) behavior of conventional alloys [183–185,187–190], there is a gap in the literature regarding the fatigue behavior of HEAs, since related studies are very rare and mostly focusing on the high-cycle fatigue(HCF) regime [191–196]. Moreover, all of these studies were established on completely different HEAs. Outstanding fatigue properties were achieved in an UFG $Al_{0.3}CoCrFeNi$ HEA through nanotwin nucleation [191]. Recent studies focusing on the HCF behavior have reported the effect of grain size on the cyclic deformation response (CDR) of the CoCrFeMnNi HEA, where UFG material possessed a considerably higher fatigue strength and stability relative to the coarse grained(CG) variant [192]. Different authors have investigated the CDR of various HEAs. Despite the fact that $Fe_{50}Mn_{30}Co_{10}Cr_{10}$ HEA has exhibited an appreciable work hardening in tensile tests [1], and the martensitic phase transformation governing the microstructural evolution in both monotonic and cyclic loading conditions [1,196], the martensitic transformation did not contribute to significant hardening under cyclic loading as compared to that in monotonic loading [196]. Coarsegrained (CG) CoCuFeMnNi HEA has also shown a lack of hardening under cyclic loading, nonetheless, in this particular HEA, phase transformation was absent and the microstructural evolution was governed by dislocation activity [195]. According to numerous studies established inthe last two decades, in the HCF regime, the fatigue strength of the UFG alloys is relatively high as compared to their CG counterparts, which is attributed to their magnificently enhancedmonotonic strength [197–200]. In contrast, in the LCF regime, fatigue lives were lower in several studies [201–205]. A good explanation for this LCF response is the localized crack initiation stemming from inhomogeneities due to insufficient material flow during SPD [206,207]. Moreover, it is important to know that crack initiation and crack propagation lives are both included in the total fatigue life. Based on that, it was reported by several researchers that SPD processed materials possess good crack initiation resistance, yet endure rapid crack propagation [208,209]. In many LCF studies conducted on different UFG alloys, it was shown that dynamic recrystallization, dislocation rearrangement and accompanying damage localization resulted in inferior fatigue strengths at low temperatures and small cycle counts [210–215]. One effective way to attain a stable UFG microstructure and CDR is to reduce the amounts of interstitials and produce precipitates [212,213]. Grain refinement using ECAP was found to remarkably extend the fatigue life at the loweststrain amplitude, whereas CG samples had better fatigue properties at higher strain amplitudes [197]. This behavior of ECAP samples could be related to cyclic softening, damage localization, aswell as the higher stress amplitudes enforced by grain refinement.

1.3. OBJECTIVES AND OUTLINE

The purpose of the present research is to obtain a clear understanding on the relationship between macroscopic mechanical behavior and microscopic deformation factors (crystallographicorientation, testing temperature, and chemical composition dependence) in M/HEAs. The study aims mainly at achieving a better understanding of the deformation mechanisms responsible for the outstanding properties of M/HEAs. For SC specimens, we will focus on [001], [111] and [123]orientations. It is convenient to choose these three crystallographic orientations in order to represent different zones of the stereographic triangle, and thus to make a number of slip and twinning systems at different stages of deformation, and most importantly observe the orientation dependence of twinning and how it evolves with strain. Additionally, both tensile and compressive loads will be applied to different specimens in order to understand influence of load direction on the mechanical deformation mechanisms. The single crystals are clearly advantageous in terms ofthe achievable fundamental understanding of deformation mechanisms, owing to the absence of grain boundaries and texture effects associated with polycrystalline materials.

The overall objectives of our study can be stated as the following:

1. Experimentally inspect the response of single crystalline NiCoCr to uniaxial load as a function of crystallographic orientation.
2. Elucidate microstructural evolution and deformation mechanisms, including twinning, slip and martensitic transformation, and their reciprocal interactions on the mechanical response of NiCoCr single crystals.
3. Generalize the outcomes and expand our material design space to other M/HEAs possessing similar characteristics. This will be helpful in designing new materials that not only have the same beneficial properties possessed by our alloys but also outperform them in some aspects.

CHAPTER 2

EXPERIMENTAL METHODS

This chapter covers the metallurgy of specimens, including single crystal development, heat treatment, test specimen morphology, and techniques for characterizing them both before and after testing. Many of tests were repeated or reproduced from the previous studies [216].

2.1. MATERIALS

Production of single crystals of M/HEAs was done using the Bridgman method in an inert helium atmosphere at tomsk state university in russia. After crystallizing, they were quenched in water at room temperature after being homogenized for 24 hours at 1473 k in an inert atmosphere. Imr test labs, lansing, new york, determined the material compositions. In accordance with astm e 1019-18, inert gas fusion thermal conductivity was used to calculate the specimens' carbon contents. Laue back-reflection pictures were used to establish the bulk crystal's orientation. Using wire electrical discharge machining (edm), dog bone-shaped tensile specimens were cut from the single crystals so that their tensile axes were along the [111], [110], and [001] crystallographic orientations. These orientations were chosen to maximize the schmid factors for slip and twinning and to trigger slip-or-twinning-biased deformation mechanisms. For the mentioned orientations, the schmid factors for slip and twinning as well as the number of the most favorable slip/twinning systems with the same schmid factors are shown in Table 2. The number falls within the range of 1 to 8. The table indicates that the preferred deformation mechanism is dependent on the crystallographic orientation based on the schmid factor assessment.

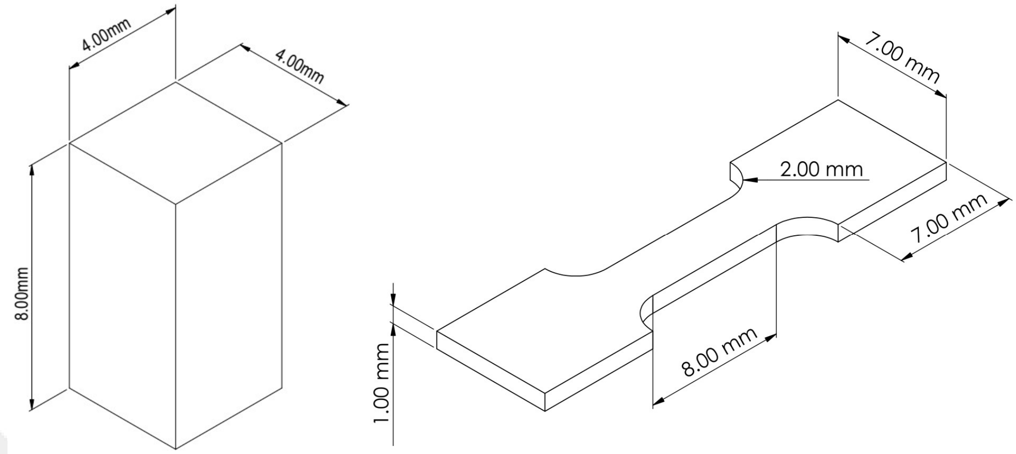

Figure 22. Tensile and compressive tests specimens' designs.

2.2. UNIAXIAL TENSILE TEST RESULTS

Prior to tensile testing, the samples were mechanically polished using a sequence of metallographic grinding papers, the coarsest of which was 800 grit. A 0.1 µm diamond solution was then used to provide a final surface finish. Using an effective strain rate of 5x10-4 s-1, room temperature uniaxial tension tests were carried out on a servohydraulic mts machine fitted with a specifically made grasping mechanism [karaman tz]. The gage section of the tension specimens measured 8 mm by 3 mm and had a thickness of 1.0 to 1.2 mm (

Figure 22). The selection of this low strain rate was made to minimize any potential rate impacts. The compression specimens were cut into 4-by-4-by-8-millimeter rectangular prisms (

Figure 22). The compression tests were conducted using tungsten carbide platens. During compression testing, thick teflon tapes were placed between the sample and the plates to reduce friction as much as possible. An mts extensometer that was fixed to the specimens' gage section was used to measure strains, and a load cell was used to measure loads. To ensure accuracy, all tests were repeated four times. To investigate the single crystals' microstructural evolution, several tests were interrupted at various strain levels prior to failure. Tests for nanoindentation were conducted using the hysitron ti 950 triboindenter. Maximum load was 10000 µn. From 150 indentations, the average nanoindentation hardness values were calculated, along with the accompanying ±standard deviations. To monitor the progression of local strain and determine the location of strain at different degrees of macro-scale deformation, in situ 2-d dic was employed. The polished surfaces were first sprayed with an adhering coating of black paint to create the background layer, and then white paint was airbrushed on top to create a fine speckle pattern. The reference and distorted states of the surfaces were captured in high-resolution photographs using an optical keyence vhx-600 microscope (4800 x 3600 pixels). Pictures were taken every five seconds. Moreover, strain localization at different phases of deformation was distinguished and the number of active deformation systems was determined using better resolution ex situ dic. An open source 2d matlab tool called ncorr was used to analyze the obtained dic pictures.

2.3. TRANSMISSION ELECTRON MICROSCOPY

A 200kv transmission electron microscope (tem) from fei, the tecnai 20st, was used to examine microstructural characteristics. On the titan themis 300 s/tem (running at 300kv), energy-filtered tem studies were carried out to reduce the signal-to-noise ratio of the diffraction contrast from the current sro [50,132] and hrtem observations. The samples were ground to a thickness of 50 to 70 µm in order to manufacture the tem foils. These foils were then twin-jet electropolished at -20°c using an electrolyte that included 80% methanol and 20% nitric acid at 10 v.

CHAPTER 3

ON THE ORIGIN OF STRAIN-HARDENING BEHAVIOR OF SINGLE CRYSTALLINE NiCoCr MEDIUM ENTROPY ALLOY

The engineering stress - strain responses and the strain-hardening response coefficient θ (dσ/dε) - true strain curves obtained from the room temperature uniaxial tension experiments are shown in

Figure 23 The [111]-oriented samples had the highest ultimate tensile strength (UTS) of 645±5 MPa over 60% strain, whereas the [110]-oriented crystals exhibited an UTS of 470±5 MPa (similar to the previous results [3]), combined with a large uniform elongation of over 120%. The highest strain-hardening coefficient was observed in the [111]- oriented crystals with 675 MPa strength and. The [001] orientation presented the lowest UTS, strain and strain hardening coefficient compared to the other orientations. All orientations demonstrate an increasing hardening rate at the beginning of the deformation with multi-deformation mechanisms activated (see optical image insets in

Figure 23). We also noted that all orientations display Luder`s type propagation of localized deformation The variations in hardening response are governed by different types and numbers of active deformation mechanisms, as described below. Clearly, the plastic flow behavior in these HEA single crystals are highly dependent on the crystallographic orientation, similar to single crystals of medium entropy alloys [3], low SFE stainless steels [217] and Hadfield steels [56,218–224].

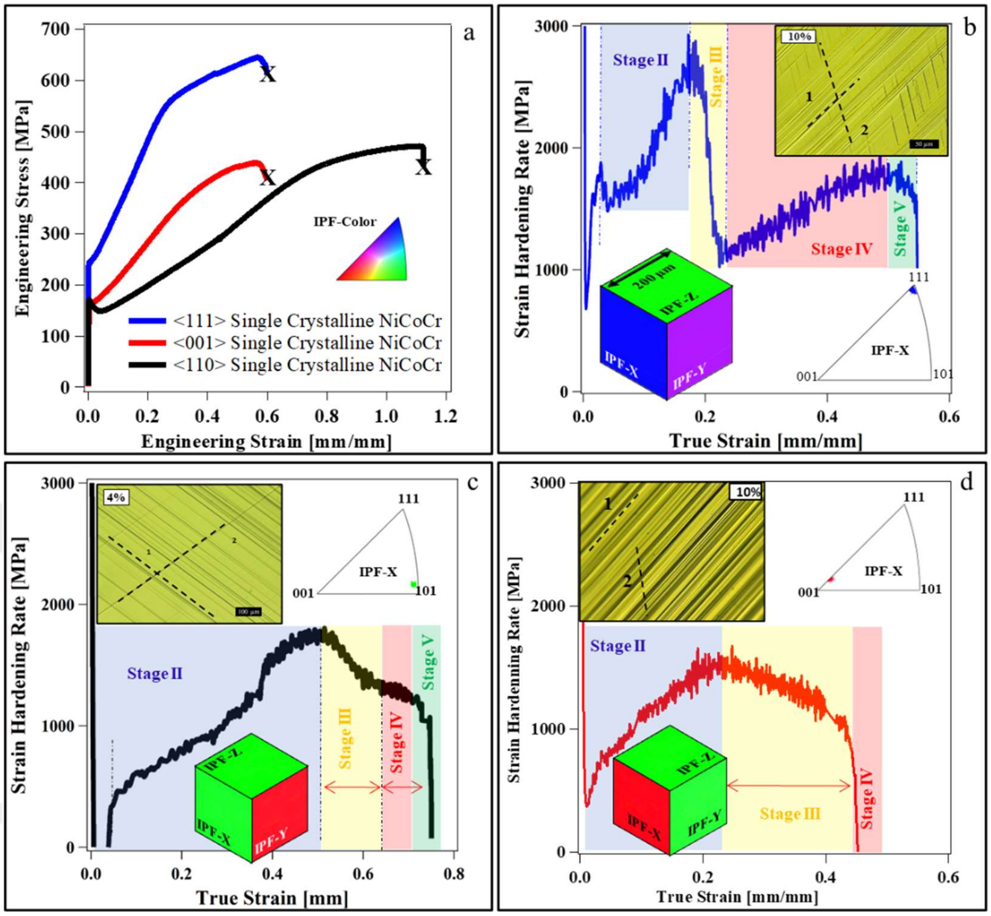

Figure 23. a) The room temperature engineering stress - engineering strain tension responses of the [111], [110]- and [001]-oriented single crystals of the NiCoCr MEA. The evolution of θ ($d\sigma/d\varepsilon$), with true strain for the b) [111], c) [110] and d) [123]-oriented crystals. Inverse pole figures and 3D schematics inset show the initial loading directions (IPFX) for three orientations, measured using EBSD. The stages of deformation were also marked for each orientation.

The strain-hardening response of NiCoCr along [110]- and [111- oriented specimens exhibits five stages, as shown in

Figure 23b and 1c, whereas the [001]-oriented crystal presents four stages. To characterize the deformation behavior of NiCoCr single crystals, samples with different loading direction were exposed to EBSD experiments after uniaxial tensile loading. The crystallographic texture measurements of bulk samples using EBSD confirmed the presence of twins and ε- martensite as observed in TEM (see supplemental

Figure 24a-e). The EBSD maps micrographs also showed two primary and tertiary twin systems inside a primary twin in the [110]-oriented failed specimen. In

Figure 24, the EBSD measurements of the [111], [110]- and [001] single crystals show a typical FCC single crystal pattern along the [110] zone axis. The EBSD IPFX maps for the sample of the [001]-oriented crystal deformed to failure shows that the plastic flow is governed by dislocation plasticity during the deformation, while the primary twinning system is activated in stage II hardening in the [111]-oriented crystal. Moreover, the secondary twinning system is observed in the stage IV, which is the main reason for an extended hardening stage as compared to the [100]-oriented crystal. The EBSD pattern of the [110] oriented crystal exhibits the twinning activity at the beginning for the deformation (stage II), while it presents elongated stripes instead of narrow spots in the stage IV (

Figure 24**)**, demonstrating the loss of single crystallinity after deformation. The distribution of these stripes indicates the secondary twin variants. The stress levels for the onset of slip (i.e., initial yield point) and twinning/ε-martensite (first confirmed by STXRD and TEM) were identified. Using these stress levels, the critical resolved shear stresses (CRSS) for dislocation glide and twinning / ε-martensite were calculated as 69±2 and 79±5 MPa, respectively, using $\tau_{cr}^{sl} = m_{sl}\sigma_{\varepsilon}^{sl}$ for slip and $\tau_{cr}^{tw} = \sigma_{\varepsilon}^{tw} m_{tw}$ for twinning.

It was shown that similar to low-SFE TWIP steels [56,225], the sharp change in stage-I hardening is due to dominant single slip and stable dislocation generation

Figure 23**a**. The dissociation of perfect dislocations into Shockley partials, followed by either the incubation stage of twinning nucleation or ε-martensitic phase transformation, are other possible factors contributing to the sharp θ decrease in stage I [111]. On the other hand, the rapid change in stage II work-hardening is believed to be driven by multiple-active deformation mechanisms, i.e., mechanically-induced twinning nucleation [3], ε-martensite [57], and dislocation activity, see

Figure 24 and

Figure 25 The existence of twin boundaries or ε-martensite in stage-II cause a reduction in dislocation mean free path through the decrease in inter-twin distances. This leads to a dynamic Hall-Petch hardening, and eventually to very high θ in stage-II. The noticeable θ reduction in stage-III was attributed to an increase in dislocation activity since a new twinning system activation is not observed via in-situ STXRD experiments.

As the twinning proceeds in stage II, more stress is needed to continue twinning and transformation. Therefore, the stage-III work-hardening acts as an incubation stage, with the formation of cell structures and Taylor lattice, [84,111] for stage IV hardening in NiCoCr in the [111]- and [110]-oriented crystals, before reaching the onset of necking. The hardening rate starts to increase in stage IV due to further dynamic Hall-Petch effect enabled by the simultaneous TWIP and TRIP mechanisms activated by LC locks and stair-rod dislocations.

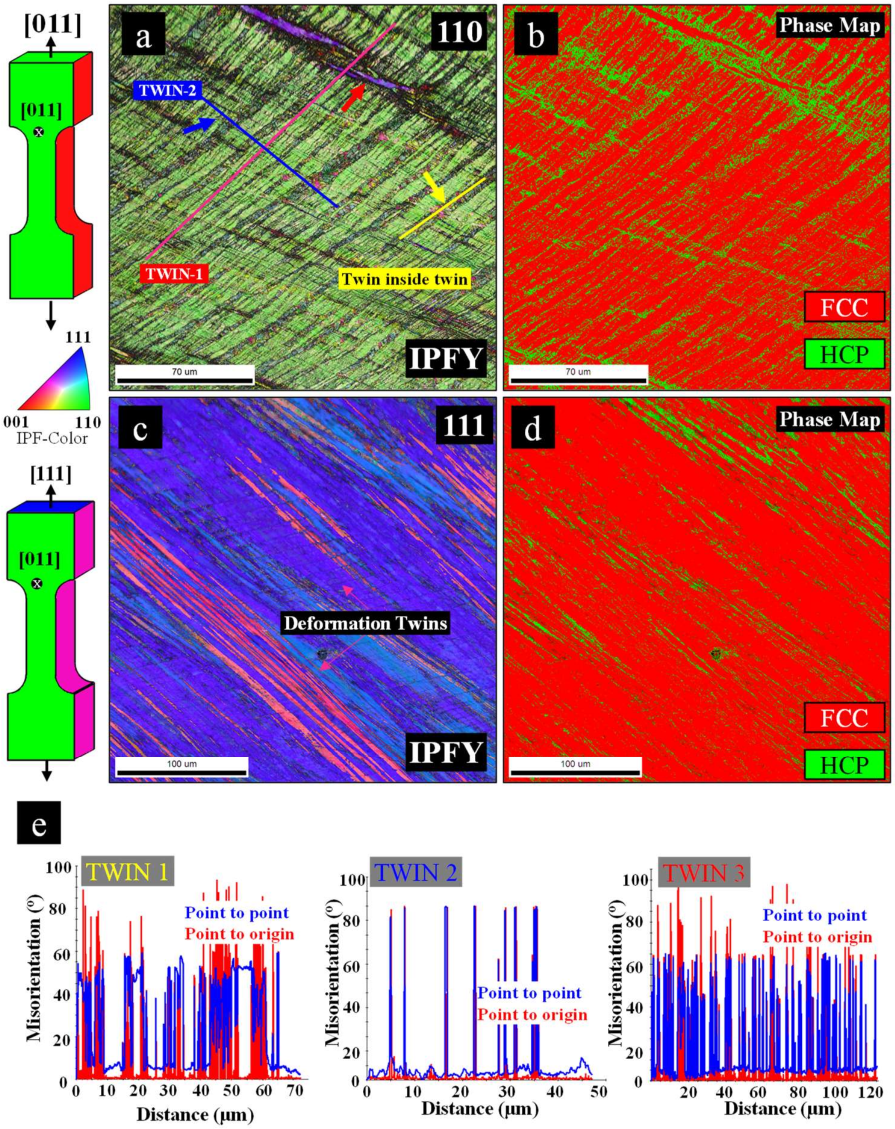

Figure 24. Representative EBSD ipf color maps illustrate microstructure of single crystalline nicocr samples deformed up to failure. a) the [110]-oriented single crystal deformed up to failure showing the twinning formation, b) ε-martensite, c) the [111]-oriented single crystal deformed up to failure indicating the deformation twinning formation d) ε-martensite. € misorientations maps proving the existence of three different twin systems marked on a).

EBSD micrograph demonstrated the existence of primary twin system in the [111] oriented sample on the microscopic scale strained up to failure. TEM pictures revealed that the twinning and hcp phase were accounted by the 1/6⟨112⟩ Shockley partial dislocations and stair-rod dislocations in in the previous studies [3,100]. The twinning and hcp phase transformation is not due to the TEM thin foil effects as both mechanisms were confirmed in bulk samples using X-Ray scans and crystallographic texture measurements (

Figure 25). X-Ray diffraction analysis of the [111] oriented single-crystal NiCoCr MEA after failure demonstrated additional hcp peak (

Figure 25a). Crystallographic texture analysis of (220) poles for the fcc crystal and the texture analysis of $(\bar{1}010)$ poles for the hcp crystal are presented in (

Figure 25b).

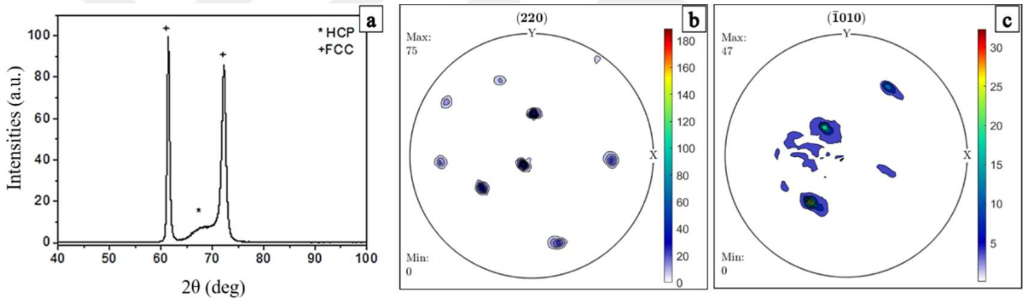

Figure 25. a) X-Ray diffraction analysis of the [111] oriented single-crystal NiCoCr MEA after failure showing additional hcp peak, b) crystallographic texture analysis of (220) poles for the fcc crystal c) the texture analysis of $(\bar{1}010)$ poles for the hcp crystal.

3.1. DETECTION OF SHORT-RANGE ORDERING (SRO)

One of the simplest experimental indication for the existence of SRO and its effect on mechanical behavior is the observation of planar slip, dislocation pile-ups and non-equivalent distance between the initial adjacent pairs of dislocations in the pile-up and the later pairs [87,226,227]. According to Cohen and Fine [88], due to the favorable (stable) SRO, the first dislocation in the pile up is exposed to higher resistance against slip due to interaction with the SRO. Once the SRO is destroyed with the passage of this dislocation, the deformation becomes localized leading to a pile-up. All successive dislocations, produced by the activated dislocation source and moving along the regions with SRO that was locally destroyed (due to rearrangement of solute) help to overcome the higher resistance. Therefore, the distance between the first and second dislocations in the pile up should be much lower as compared to the distance between the successive dislocations [87,226,227].

Hence, it is used [110]- and [111]-oriented single-crystal NiCoCr bulk samples and uniaxially deformed them at RT to observe the effect of SRO on TWIP/TRIP. We have chosen single crystals to better understand the deformation mechanisms by eliminating confounding factors such as grain boundaries and grain-size strengthening prevalent in polycrystalline samples. The rationale for choosing these two crystallographic orientations is to sample different regions of the stereographic triangle and to form different numbers of slip and twinning systems at various stages of deformation. In addition, it can be monitored the orientation dependence of the strain level at which the mechanisms initiate, and how TWIP and TRIP evolve.

Transmission Electron Microscopy (TEM) investigations on a [110]-oriented sample strained up to 4% under tension confirm the above mechanisms and thus the existence of SRO. The observations (

Figure 26 a-b) qualitatively matches with the previous studies. The first two dislocations in the pile-ups are much closer than others (

Figure 23a), a clear signature of SRO in single crystalline NiCoCr medium entropy alloy.

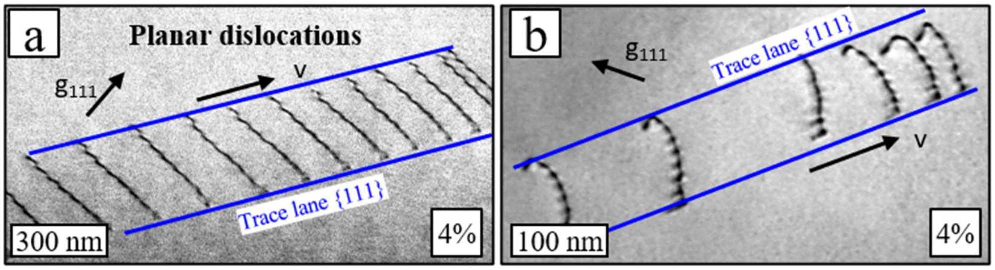

Figure 26. Bright-field TEM images of the [110]-oriented single crystals after tensile deformation at RT up to 4% strain, showing (b-c) a planar dislocation pile-up on a single slip system with non-equivalent distances between the dislocations at the pile-up tip.

To investigate short-range order (SRO) in NiCoCr single crystals, Sezer et al., performed high-resolution transmission electron microscopy (HRTEM) [100]. Two NiCoCr single crystalline samples were exposed different heat treatments following homogenization at 1473 K: (1) water-quenched to room temperature (WQ, referred to as "as-quenched"), and (2) aged at 1273 K for 48 hours, followed by furnace cooling (denoted as "aged-48h"). The microstructure and SRO characteristics were examined using energy-filtered and high-resolution TEM imaging, as shown in

Figure 27 The energy-filtered [110] electron-diffraction patterns reveal streaking along the {111} directions between Bragg spots in the aged-48h sample (

Figure 27b), while no significant streaking is observed in the WQ sample (

Figure 27a). Quantitative analysis of the diffuse scattering intensity along the dashed lines in

Figure 27a and

Figure 27b is also provided. By placing the objective aperture at the centers of the (000) and {111} spots, highlighted by the blue circles in

Figure 27a and

Figure 27b, SRO is visualized as bright dots in energy-filtered, dark-field TEM images (

Figure 27c and

Figure 27d). The aged-48h sample exhibits a high density of nanoscale domains (~5-7 nm), while smaller (~2 nm) nano-domains are sporadically present in both the WQ and aged-48h samples, suggesting that SRO is in a nascent state in the WQ sample. High-resolution TEM images and corresponding Fast Fourier transforms (ffts) for the WQ and aged-48h samples are compared in

Figure 27e and

Figure 27f. The WQ sample displays a mostly uniform fcc structure with minimal defects, whereas the aged-48h sample shows superlattice features of approximately 5 nm along {111} planes (highlighted by white circles in

Figure 27f), aligning with the size of the nano-domains observed in energy-filtered, dark-field images. These findings suggest that high-temperature aging enhances the formation of SRO in the single-crystalline NiCoCr samples. These experimental investigations support our findings in

Figure 26 They also investigated directly effect of SRO mechanical behaviors in NiCoCr.

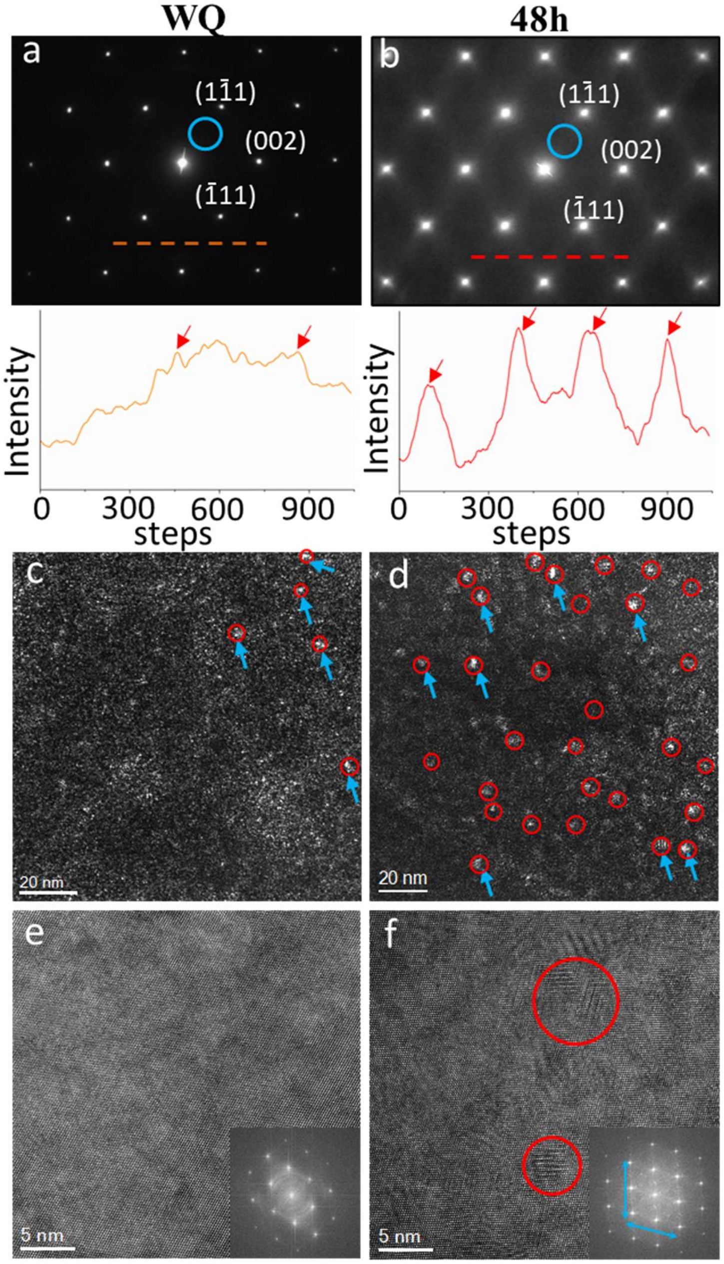

Figure 27. The microstructure of water-quenched (WQ, left panel) and 1273 K / 48 h aged (48 h, right panel) samples is shown. (a, b) display energy-filtered diffraction patterns taken along the [110] zone axis for the WQ and 48h samples, respectively. Streaks along the {111} directions are visible only in the 48h sample, as confirmed by the intensity line profile along the dashed lines in the diffraction pattern below. (c, d) show energy-filtered dark-field images of the WQ and 48h samples, with aperture positions marked by blue circles in a) and b). In the 48h sample d), short-range ordered domains (bright dots marked by red circles and blue arrows) ranging from ~2 nm to ~7 nm in size are extensively observed, unlike in the WQ sample. (e, f) present typical high-resolution TEM images and corresponding fast Fourier transform (FFT) images for the WQ and 48h samples. The WQ sample exhibits a mostly uniform structure,

while the 48h sample reveals superlattice features (indicated by red circles in f)). Streaking along the {111} directions is also visible in the FFT pattern of the 48h sample f), indicated by blue arrows [100].

3.2. EFFECT OF SHORT-RANGE ORDERING ON THE MECHANICAL PROPERTIES

To examine the impact of SRO on mechanical behavior, uniaxial tensile tests were conducted on both as-quenched and aged single-crystal samples at room temperature (RT) [100]. The tensile test results show that while aging for 48 hours increases the degree of SRO, it leads to only a slight improvement in yield strength (around 6% ± 3%) across all orientations, consistent with previous theoretical predictions [94]. However, a significant enhancement in true strain (~15% ± 2% for [111]-oriented crystals and ~25% ± 2% for [110]-oriented crystals) and ultimate true-tensile strength (~15% ± 2% for [111] and ~30% ± 2% for [110]) was observed in aged samples for both [111] and [110] orientations, while the stress-strain responses of the as-quenched and aged samples in the [001] orientation showed no notable differences in this study [100].

The marked improvement in tensile ductility in the aged samples is attributed to the increased degree of SRO. To further explore how SRO influences deformation mechanisms, EBSD maps were recorded in uniformly deformed regions before necking for the [111], [110], and [001] single-crystal tensile specimens. EBSD imaging revealed that the superior strength and ductility in the aged samples are due to a higher density of strain-induced twinning and ε-martensite formation in both [111] (

Figure 28a) and [110] (

Figure 28b) orientations. The increased SRO likely delays recovery processes, thereby enhancing the TWIP/TRIP effects by raising stress levels and influencing partial dislocation separation [3,84,85,216]. In contrast, no twinning or ε-martensite was detected in the [001] orientation according to EBSD imaging.

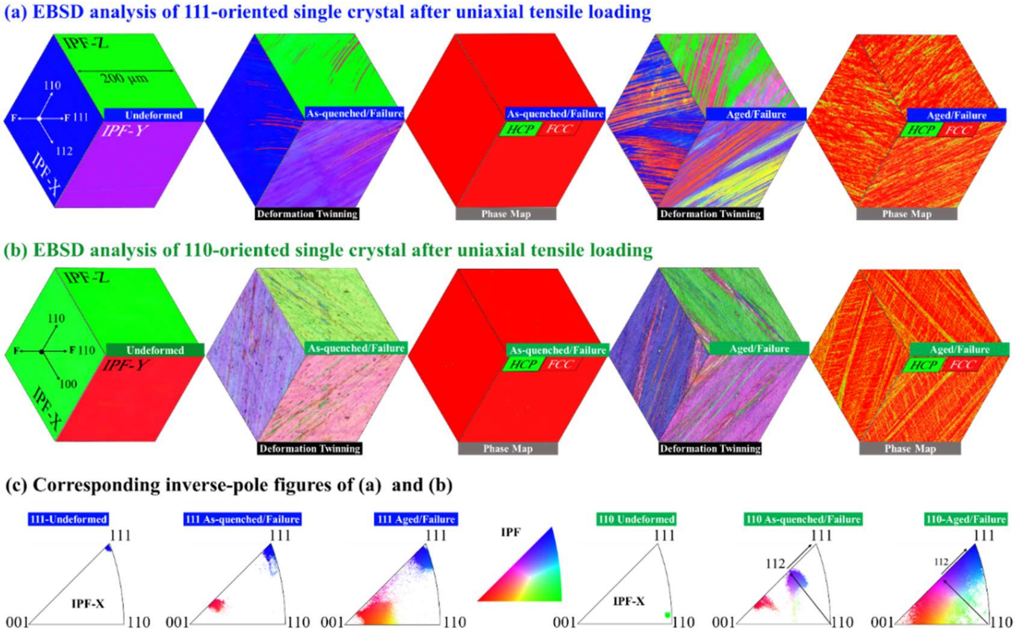

Figure 28. Representative EBSD IPF color and phase maps provide a visual overview of the microstructure in single-crystalline NiCoCr specimens. In a), the [111]-oriented, and in b), the [110]-oriented single crystals are shown in their initial as-quenched conditions, deformed to failure, illustrating the formation of twinning and ε-martensite. For the 48-hour aged samples, also deformed to failure, an increased density of twins and ε-martensite is observed. c) displays the corresponding inverse pole figures for the [111]- and [110]-oriented crystals shown in a) and b) [100].

A recent study on the influence of SRO on the mechanical response of NiCoCr along the [123] orientation similarly found no improvement in tensile ductility, akin to the results for the [001]-oriented crystal in this study [107]. This is because the [123] orientation lies near the center of the stereographic triangle, where the applied stress has little effect on partial dislocation separation and stacking fault energy [3,84,85,216], limiting twinning, martensitic transformations, and changes in deformation modes under higher stress levels. The Schmid factors for slip and twinning, experimental yield strengths, and critical resolved shear stress values are listed in Table 2 These results clearly demonstrate that SRO directly influences the TWIP/TRIP effects.

3.3. COMPARISON OF MECHANICAL TENSILE TESTS OF MEDIUM AND HIGH ENTROPY ALLOYS WITH CONVENTIONAL STEELS

$Fe_{40}Mn_{40}Cr_{10}Co_{10}$ HEA, NiCoCr MEA and many other M/HEAs exhibit one of the highest strain hardening behaviors among other HEAs. However, the underlying secrets were still mysterious and needed to be revealed by studying single crystalline version of the alloys, in order to eliminate grain boundaries and texture effects. Therefore, Sezer et al. [84] made a research on single crystalline $Fe_{40}Mn_{40}Cr_{10}Co_{10}$ HEA in different crystallographic directions, and compared them with two TWIP steels, namely Hadfield and SS316 steel, which exhibit superior strain hardening behavior. The three directions which he chose were [001], [111] and [123]. In the [111] orientation, the alloy exhibited a strain hardening behavior similar to TWIP steels, which also possess low sfes [37,45,54]. However, the [001] and [123] oriented specimens were not very similar to the [111] specimens, as they did not show as remarkable strain hardening behavior comparing to TWIP steel single crystals oriented in the same directions.

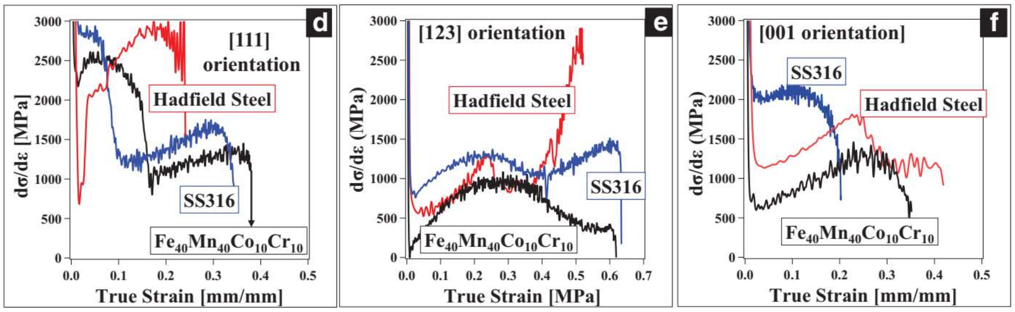

Figure 29. Comparison of the strain hardening rate responses of $Fe_{40}Mn_{40}Cr_{10}Co_{10}$ HEA, Hadfield steel and SS316 stainless steel, obtained from uniaxial tension at room temperature [84].

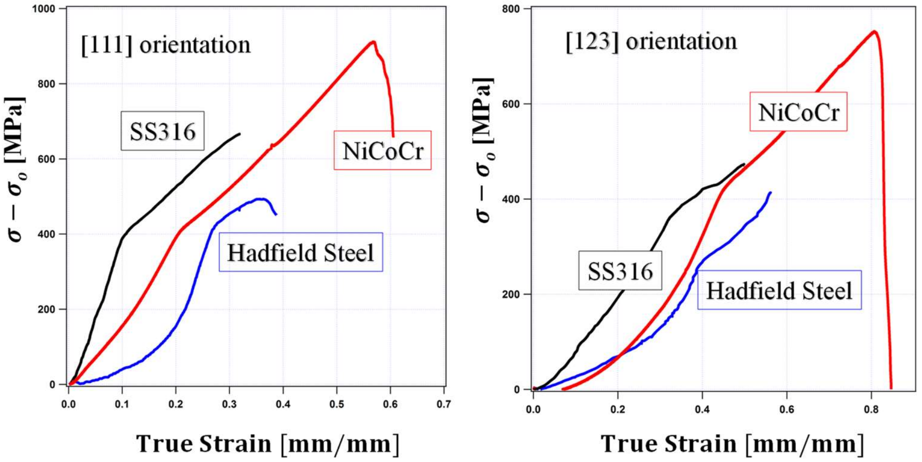

Figure 30. The comparison of strength differentials (σ - σ₀, where σ₀ is the yield strength) and hardening response as a function of applied strain is shown for three medium to low stacking fault energy materials: 316 stainless steel (SS316) [28], Fe-12%Mn-1%C Hadfield steel [21], and the current medium entropy NiCoCr alloy. This comparison highlights the superior ductility and strength differential of the NiCoCr alloy, which demonstrates a more pronounced hardening response and better mechanical performance compared to SS316 and Hadfield steel under similar strain conditions [3].

The uniaxial tensile responses of the three different orientations of equiatomic NiCoCr medium entropy alloy (MEA) single crystals investigated in this study closely resemble those observed in 316L stainless steel [55] and Fe-12%Mn-1%C Hadfield steel [56] single crystals, particularly regarding the hardening response, stages of deformation, and relative hardening rates. However, a key difference is that the steels exhibit higher yield strengths, as their critical resolved shear stresses (CRSS) are greater than that of the NiCoCr MEA. Despite this, the NiCoCr MEA crystals show significantly greater ductility—more than 50% higher than the steels.

A notable distinction between the NiCoCr MEA and 316 stainless steel/Hadfield steel single crystals lies in the extent of Stage IV hardening in the orientations examined ([111], [123], and [110]). In NiCoCr single crystals, the combined strain levels for Stage III and Stage IV are considerably higher than those in 316 stainless steel and Hadfield steel. This suggests that secondary twinning and/or the formation of twin networks during Stage IV deformation in NiCoCr crystals play a critical role in suppressing necking and enhancing ductility. One possible explanation is that the twins in NiCoCr appear to be thinner compared to those in 316 stainless steel and Hadfield steel during Stage IV, which may create more boundaries for slip interactions. This suggests that NiCoCr has a greater capacity for dislocation storage and better resistance to necking instability than these conventional low and medium stacking fault energy (SFE) steels.

CHAPTER 4

CONCLUSIONS

In this study, single crystals of NiCoCr were examined to reveal the influence of short-range ordering (SRO) and crystal orientation on their mechanical behavior $Fe_{40}Mn_{40}Co_{10}Cr_{10}$, CoCrFeMnNi medium/high entropy alloys (M/HEAs). Various crystallographic orientations were systematically investigated, along with the low-cycle fatigue behavior at different strain amplitudes (0.2%, 0.4%, and 0.6%) for both single and polycrystalline HEAs. The main findings are as follows:

1. Strain Hardening and Orientation Dependence: The strain hardening response and strain hardening coefficient at room temperature under tension show a strong dependence on crystallographic orientation in both NiCoCr MEA and Fe40Mn40Co10Cr10 HEA. This behavior is influenced by the activation of orientation-specific deformation mechanisms, such as deformation twinning and planar slip, as well as the formation of dislocation networks or walls. In the [011], [111], and [123] orientations, four distinct stages of strain hardening occur due to the activation of multiple twin systems, while the [001] orientation shows only three stages, lacking deformation twinning.

2. Exceptional Strain Hardening in the [111] Orientation: The [111] orientation in both NiCoCr MEA and Fe40Mn40Co10Cr10 HEA displayed an outstanding strain hardening coefficient (θ), attributed to the activation and interaction of multiple twin systems during stage 2 of deformation. The high ductility in this orientation, despite its significant strength, was due to the formation of nano-twins within primary twins and the activation of tertiary twins in stage 4, which provided additional deformation when other mechanisms were exhausted. Additionally, multiple slip mechanisms in the [111] orientation allowed Shockley partial dislocations to form stacking faults in stage 4. This response

is similar to twinning-induced plasticity (TWIP) steels with low stacking fault energy. For the [123] orientation, deformation was dominated by planar slip, with the coexistence of slip and nano-twins in stage 2 contributing to strain hardening. Unexpectedly, the [123] orientation also exhibited stage 4 hardening, similar to the [111] orientation, due to deformation twinning and dislocation structures forming in stage 4.

3. Lack of Twinning in the [001] Orientation: In NiCoCr MEA, Fe40Mn40Co10Cr10 HEA, and CoCrFeMnNi HEA, no twinning was observed in the [001] orientation, which aligns with the Copley-Kear effect for interstitial-free face-centered cubic (fcc) metals. Strain hardening in this orientation was attributed to the formation of high-density dislocation walls (HDDWs) along multiple slip systems. Although planar slip is typically associated with HDDW formation, planar features were not observed in transmission electron microscopy (TEM) of the [001] orientation. Instead, dislocation interactions, including the formation of multi-junctions and dislocation dipoles, facilitated the development of HDDWs, which acted as barriers to dislocation motion and formed a structure similar to a Taylor lattice, enabling dislocation cell formation.

4. Comparison with Low Stacking Fault Energy Steels: The strain hardening response of the M/HEAs in this study was compared to conventional low stacking fault energy steels, such as 316 stainless steel and Hadfield steel. Although the M/HEAs lack interstitial solid solution hardening, they exhibit similar strain hardening stages to these steels. However, M/HEAs demonstrate higher ductility in the [111] and [123] orientations due to extended stage 4 hardening, though they have lower yield strength compared to 316 stainless steel and Hadfield steel. In the [001] orientation, the conventional steels displayed better plastic deformation ability due to deformation twinning.

5. Role of SRO in Deformation Modes: While previous studies on conventional steels and M/HEAs primarily focused on stacking fault energy, recent studies

highlight the direct influence of SRO on deformation mechanisms. This discovery is significant for designing new MPEAs with enhanced plastic deformation capabilities. Despite this progress, further research is necessary to fully understand the complex nature of SRO and its interactions with phase transformation nucleation mechanisms.

REFERENCE

[1] Z. Li, K.G. Pradeep, Y. Deng, D. Raabe, C.C. Tasan, Metastable high-entropy dual-phase alloys overcome the strength–ductility trade-off, Nature 534 (2016) 227–230.

[2] R. Seede, B. Zhang, A. Whitt, S. Picak, S. Gibbons, P. Flater, A. Elwany, R. Arroyave, I. Karaman, Effect of heat treatments on the microstructure and mechanical properties of an ultra-high strength martensitic steel fabricated via laser powder bed fusion additive manufacturing, Addit. Manuf. 47 (2021) 102255.

[3] B. Uzer, S. Picak, J. Liu, T. Jozaghi, D. Canadinc, I. Karaman, Y.I. Chumlyakov, I. Kireeva, On the mechanical response and microstructure evolution of NiCoCr single crystalline medium entropy alloys, Mater. Res. Lett. 6 (2018) 442–449.

[4] B. Gludovatz, A. Hohenwarter, D. Catoor, E.H. Chang, E.P. George, R.O. Ritchie, A fracture-resistant high-entropy alloy for cryogenic applications, Science (80-.). 345 (2014) 1153–1158.

[5] B. Gorr, M. Azim, H.-J. Christ, T. Mueller, D. Schliephake, M. Heilmaier, Phase equilibria, microstructure, and high temperature oxidation resistance of novel refractory high-entropy alloys, J. Alloys Compd. 624 (2015) 270–278.

[6] C. Niu, C.R. LaRosa, J. Miao, M.J. Mills, M. Ghazisaeidi, Magnetically-driven phase transformation strengthening in high entropy alloys, Nat. Commun. 9 (2018) 1363.

[7] Y. Qiu, S. Thomas, M.A. Gibson, H.L. Fraser, N. Birbilis, Corrosion of high entropy alloys, Npj Mater. Degrad. 1 (2017) 15.

[8] J.W. Yeh, Recent progress in high-entropy alloys, Ann. Chim. Sci. Des Mater. 31 (2006) 633–648.

[9] Y. Zhang, T.T. Zuo, Z. Tang, M.C. Gao, K.A. Dahmen, P.K. Liaw, Z.P. Lu, Microstructures and properties of high-entropy alloys, Prog. Mater. Sci. 61 (2014) 1–93.

[10] Y. Zhang, X. Yang, P.K. Liaw, Alloy Design and Properties Optimization of High-Entropy Alloys, JOM 64 (2012) 830–838.

[11] J.-W. Yeh, S.-K. Chen, S.-J. Lin, J.-Y. Gan, T.-S. Chin, T.-T. Shun, C.-H. Tsau, S.-Y. Chang, Nanostructured High-Entropy Alloys with Multiple Principal Elements: Novel Alloy Design Concepts and Outcomes, Adv. Eng. Mater. 6

(2004) 299–303.

[12] D.B. Miracle, O.N. Senkov, A critical review of high entropy alloys and related concepts, Acta Mater. 122 (2017) 448–511.

[13] Y. Qiu, Y.J. Hu, A. Taylor, M.J. Styles, R.K.W. Marceau, A. V Ceguerra, M.A. Gibson, Z.K. Liu, H.L. Fraser, N. Birbilis, A lightweight single-phase AlTiVCr compositionally complex alloy, Acta Mater. 123 (2017) 115–124.

[14] X.-W. Qiu, Y.-P. Zhang, L. He, C. Liu, Microstructure and corrosion resistance of AlCrFeCuCo high entropy alloy, J. Alloys Compd. 549 (2013) 195–199.

[15] A. Tamm, A. Aabloo, M. Klintenberg, M. Stocks, A. Caro, Atomic-scale properties of Ni-based FCC ternary, and quaternary alloys, Acta Mater. 99 (2015) 307–312.

[16] F.X. Zhang, S. Zhao, K. Jin, H. Xue, G. Velisa, H. Bei, R. Huang, J.Y.P. Ko, D.C. Pagan, J.C. Neuefeind, W.J. Weber, Y. Zhang, Local Structure and Short-Range Order in a NiCoCr Solid Solution Alloy, Phys. Rev. Lett. 118 (2017) 205501.

[17] Y. Ma, Q. Wang, C. Li, L.J. Santodonato, M. Feygenson, C. Dong, P.K. Liaw, Chemical short-range orders and the induced structural transition in high-entropy alloys, Scr. Mater. 144 (2018) 64–68.

[18] M. Widom, W.P. Huhn, S. Maiti, W. Steurer, Hybrid Monte Carlo/Molecular Dynamics Simulation of a Refractory Metal High Entropy Alloy, Metall. Mater. Trans. A 45 (2014) 196–200.

[19] P. Singh, A. V Smirnov, D.D. Johnson, Atomic short-range order and incipient long-range order in high-entropy alloys, Phys. Rev. B 224204 (2015) 1–12.

[20] J. Ding, Q. Yu, M. Asta, R.O. Ritchie, Tunable stacking fault energies by tailoring local chemical order in CrCoNi medium-entropy alloys, Proc. Natl. Acad. Sci. 115 (2018) 8919–8924.

[21] T. Kostiuchenko, A. V Ruban, J. Neugebauer, A. Shapeev, F. Körmann, Short-range order in face-centered cubic VCoNi alloys, Phys. Rev. Mater. 4 (2020) 113802.

[22] R. Zhang, S. Zhao, J. Ding, Y. Chong, T. Jia, C. Ophus, M. Asta, R.O. Ritchie, A.M. Minor, Short-range order and its impact on the CrCoNi medium-entropy alloy, Nature 581 (2020) 283–287.

[23] B. Gludovatz, A. Hohenwarter, K.V.S. Thurston, H. Bei, Z. Wu, E.P. George, R.O. Ritchie, Exceptional damage-tolerance of a medium-entropy alloy CrCoNi at cryogenic temperatures, Nat. Commun. 7 (2016) 10602.

[24] N.L. Okamoto, K. Yuge, K. Tanaka, H. Inui, E.P. George, Atomic displacement

in the CrMnFeCoNi high-entropy alloy – A scaling factor to predict solid solution strengthening, AIP Adv. 6 (2016) 125008.

[25] M.J. Yao, K.G. Pradeep, C.C. Tasan, D. Raabe, A novel, single phase, non-equiatomic FeMnNiCoCr high-entropy alloy with exceptional phase stability and tensile ductility, Scr. Mater. 72–73 (2014) 5–8.

[26] C.C. Tasan, Y. Deng, K.G. Pradeep, M.J. Yao, H. Springer, D. Raabe, Composition Dependence of Phase Stability, Deformation Mechanisms, and Mechanical Properties of the CoCrFeMnNi High-Entropy Alloy System, JOM 66 (2014) 1993–2001.

[27] K.G. Pradeep, C.C. Tasan, M.J. Yao, Y. Deng, H. Springer, D. Raabe, Non-equiatomic high entropy alloys: Approach towards rapid alloy screening and property-oriented design, Mater. Sci. Eng. A 648 (2015) 183–192.

[28] Y. Deng, C.C. Tasan, K.G. Pradeep, H. Springer, A. Kostka, D. Raabe, Design of a twinning-induced plasticity high entropy alloy, Acta Mater. 94 (2015) 124–133.

[29] Y.P. "Wang, H.Z. [School of M.S. and E. “Fu Harbin Institute of Technology Harbin (China)],” B.S. [School of M.S. and E. “Li Harbin Institute of Technology Harbin (China)]”, H.I. of T.H. (China)]" "Micro/Nano Technology Research Center, Solid solution or intermetallics in a high-entropy alloy, 11 (2009).

[30] L.R. Owen, E.J. Pickering, H.Y. Playford, H.J. Stone, M.G. Tucker, N.G. Jones, An assessment of the lattice strain in the CrMnFeCoNi high-entropy alloy, Acta Mater. 122 (2017) 11–18.

[31] W. Lu, C.H. Liebscher, G. Dehm, D. Raabe, Z. Li, Bidirectional Transformation Enables Hierarchical Nanolaminate Dual-Phase High-Entropy Alloys, Adv. Mater. 30 (2018) 1804727.

[32] Y. Bu, Z. Li, J. Liu, H. Wang, D. Raabe, W. Yang, Nonbasal Slip Systems Enable a Strong and Ductile Hexagonal-Close-Packed High-Entropy Phase, Phys. Rev. Lett. 122 (2019) 75502.

[33] G. Laplanche, A. Kostka, O.M. Horst, G. Eggeler, E.P. George, Microstructure evolution and critical stress for twinning in the CrMnFeCoNi high-entropy alloy, Acta Mater. 118 (2016) 152–163.

[34] K.V.S. Thurston, A. Hohenwarter, G. Laplanche, E.P. George, B. Gludovatz, R.O. Ritchie, On the onset of deformation twinning in the CrFeMnCoNi high-entropy alloy using a novel tensile specimen geometry, Intermetallics 110 (2019) 106469.

[35] S. Picak, H.C. Yilmaz, I. Karaman, Simultaneous deformation twinning and martensitic transformation in CoCrFeMnNi high entropy alloy at high

temperatures, Scr. Mater. 202 (2021) 113995.

[36] J.D. Weeks, Hadfield's Manganese Steel, Science (80-.). ns-12 (1888) 284–286.

[37] O. Grässel, L. Krüger, G. Frommeyer, L.W. Meyer, High strength Fe–Mn–(Al, Si) TRIP/TWIP steels development — properties — application, Int. J. Plast. 16 (2000) 1391–1409.

[38] X. Wu, M. Yang, F. Yuan, G. Wu, Y. Wei, X. Huang, Y. Zhu, Heterogeneous lamella structure unites ultrafine-grain strength with coarse-grain ductility, Proc. Natl. Acad. Sci. 112 (2015) 14501–14505.

[39] S.-H. Kim, H. Kim, N.J. Kim, Brittle intermetallic compound makes ultrastrong low-density steel with large ductility, Nature 518 (2015) 77–79.

[40] S. Mahajan, G.Y. Chin, Twin-slip, twin-twin and slip-twin interactions in Co-8 wt.% Fe alloy single crystals, Acta Metall. 21 (1973) 173–179.

[41] L. Rémy, Twin-slip interaction in f.c.c. crystals, Acta Metall. 25 (1977) 711–714.

[42] J.A. Venables, Deformation twinning in face-centred cubic metals, Philos. Mag. A J. Theor. Exp. Appl. Phys. 6 (1961) 379–396.

[43] S. MIURA, Proceedings of International Conference on Strength of Metals and Alloys, Trans. JIM. 9 (1968) 555.

[44] S. Mahajan, G.Y. Chin, Formation of deformation twins in f.c.c. crystals, Acta Metall. 21 (1973) 1353–1363.

[45] I. Karaman, H. Sehitoglu, K. Gall, Y.. Chumlyakov, H.. Maier, Deformation of single crystal Hadfield steel by twinning and slip, Acta Mater. 48 (2000) 1345–1359.

[46] I. V Kireeva, Y.I. Chumlyakov, Z. V Pobedennaya, Y.N. Platonova, I. V Kuksgauzen, D.A. Kuksgauzen, V. V Poklonov, I. Karaman, H. Sehitoglu, Slip and Twinning in the [$$ \overline{\mathbf{1}} $$49]-Oriented Single Crystals of a High-Entropy Alloy, Russ. Phys. J. 59 (2016) 1242–1250.

[47] Z. Wu, H. Bei, G.M. Pharr, E.P. George, Temperature dependence of the mechanical properties of equiatomic solid solution alloys with face-centered cubic crystal structures, Acta Mater. 81 (2014) 428–441.

[48] F. Otto, A. Dlouhý, C. Somsen, H. Bei, G. Eggeler, E.P. George, The influences of temperature and microstructure on the tensile properties of a CoCrFeMnNi high-entropy alloy, Acta Mater. 61 (2013) 5743–5755.

[49] P.P. Bhattacharjee, G.D. Sathiaraj, M. Zaid, J.R. Gatti, C. Lee, C.-W. Tsai, J.-

W. Yeh, Microstructure and texture evolution during annealing of equiatomic CoCrFeMnNi high-entropy alloy, J. Alloys Compd. 587 (2014) 544–552.

[50] W. Abuzaid, H. Sehitoglu, Critical resolved shear stress for slip and twin nucleation in single crystalline FeNiCoCrMn high entropy alloy, Mater. Charact. 129 (2017) 288–299.

[51] L. Patriarca, A. Ojha, H. Sehitoglu, Y.I. Chumlyakov, Slip nucleation in single crystal FeNiCoCrMn high entropy alloy, Scr. Mater. 112 (2016) 54–57.

[52] I. Kireeva, Y. Chumlyakov, Z. Pobedennaya, D. Kuksgauzen, I. Karaman, H. Sehitoglu, Mechanisms of plastic deformation in [1¯11]-oriented single crystals of FeNiMnCrCo high entropy alloy, AIP Conf. Proc. 1783 (2016) 20090.

[53] R. Raghavan, C. Kirchlechner, B.N. Jaya, M. Feuerbacher, G. Dehm, Mechanical size effects in a single crystalline equiatomic FeCrCoMnNi high entropy alloy, Scr. Mater. 129 (2017) 52–55.

[54] P. Chowdhury, D. Canadinc, H. Sehitoglu, On deformation behavior of Fe-Mn based structural alloys, Mater. Sci. Eng. R Reports 122 (2017) 1–28.

[55] I. Karaman, H. Sehitoglu, H.J. Maier, Y.I. Chumlyakov, Competing mechanisms and modeling of deformation in austenitic stainless steel single crystals with and without nitrogen, Acta Mater. 49 (2001) 3919–3933.

[56] I. Karaman, H. Sehitoglu, A.J. Beaudoin, Y.I. Chumlyakov, H.J. Maier, C.N. Tomé, Modeling the deformation behavior of Hadfield steel single and polycrystals due to twinning and slip, Acta Mater. 48 (2000) 2031–2047.

[57] O. Bouaziz, S. Allain, C.P. Scott, P. Cugy, D. Barbier, High manganese austenitic twinning induced plasticity steels: A review of the microstructure properties relationships, Curr. Opin. Solid State Mater. Sci. 15 (2011) 141–168.

[58] P. Singh, S. Picak, A. Sharma, Y.I. Chumlyakov, R. Arroyave, I. Karaman, D.D. Johnson, Martensitic Transformation in ${\mathrm{Fe}}_{x}{\mathrm{Mn}}_{80\ensuremath{-}x}{\mathrm{Co}}_{10}{\mathrm{Cr}}_{10}$ High-Entropy Alloy, Phys. Rev. Lett. 127 (2021) 115704.

[59] D.R. Steinmetz, T. Jäpel, B. Wietbrock, P. Eisenlohr, I. Gutierrez-Urrutia, A. Saeed–Akbari, T. Hickel, F. Roters, D. Raabe, Revealing the strain-hardening behavior of twinning-induced plasticity steels: Theory, simulations, experiments, Acta Mater. 61 (2013) 494–510.

[60] C.J. Wang, B.N. Yao, Z.R. Liu, X.F. Kong, D. Legut, R.F. Zhang, Y. Deng, Effects of solutes on dislocation nucleation and interface sliding of bimetal semi-coherent interface, Int. J. Plast. 131 (2020) 102725.

[61] Z. Wu, H. Bei, F. Otto, G.M. Pharr, E.P. George, Recovery, recrystallization,

grain growth and phase stability of a family of FCC-structured multi-component equiatomic solid solution alloys, Intermetallics 46 (2014) 131–140.

[62] A. Gali, E.P. George, Tensile properties of high- and medium-entropy alloys, Intermetallics 39 (2013) 74–78.

[63] D. Zhao, X. Ma, S. Picak, I. Karaman, K. Xie, Activation and suppression of 〈c + a〉 dislocations in a textured Mg–3Al–1Zn alloy, Scr. Mater. 179 (2020) 49–54.

[64] G. Laplanche, A. Kostka, C. Reinhart, J. Hunfeld, G. Eggeler, E.P. George, Reasons for the superior mechanical properties of medium-entropy CrCoNi compared to high-entropy CrMnFeCoNi, Acta Mater. 128 (2017) 292–303.

[65] K. Jin, Y.F. Gao, H. Bei, Intrinsic properties and strengthening mechanism of monocrystalline Ni-containing ternary concentrated solid solutions, Mater. Sci. Eng. A 695 (2017) 74–79.

[66] Y.H. Zhao, Y.T. Zhu, X.Z. Liao, Z. Horita, T.G. Langdon, Tailoring stacking fault energy for high ductility and high strength in ultrafine grained Cu and its alloy, Appl. Phys. Lett. 89 (2006) 121906.

[67] B. Gumus, B. Bal, G. Gerstein, D. Canadinc, H.J. Maier, F. Guner, M. Elmadagli, Twinning activities in high-Mn austenitic steels under high-velocity compressive loading, Mater. Sci. Eng. A 648 (2015) 104–112.

[68] J. Miao, C.E. Slone, T.M. Smith, C. Niu, H. Bei, M. Ghazisaeidi, G.M. Pharr, M.J. Mills, The evolution of the deformation substructure in a Ni-Co-Cr equiatomic solid solution alloy, Acta Mater. 132 (2017) 35–48.

[69] I. Karaman, H. Sehitoglu, Y.I. Chumlyakov, H.J. Maier, The deformation of low-stacking-fault-energy austenitic steels, JOM 54 (2002) 31–37.

[70] L. Xue, K.C. Atli, S. Picak, C. Zhang, B. Zhang, A. Elwany, R. Arroyave, I. Karaman, Controlling martensitic transformation characteristics in defect-free NiTi shape memory alloys fabricated using laser powder bed fusion and a process optimization framework, Acta Mater. 215 (2021) 117017.

[71] C.E. Slone, J. Miao, E.P. George, M.J. Mills, Achieving ultra-high strength and ductility in equiatomic CrCoNi with partially recrystallized microstructures, Acta Mater. 165 (2019) 496–507.

[72] S.S. Sohn, A. Kwiatkowski da Silva, Y. Ikeda, F. Körmann, W. Lu, W.S. Choi, B. Gault, D. Ponge, J. Neugebauer, D. Raabe, Ultrastrong Medium-Entropy Single-Phase Alloys Designed via Severe Lattice Distortion, Adv. Mater. 31 (2019) 1807142.

[73] C.E. Slone, S. Chakraborty, J. Miao, E.P. George, M.J. Mills, S.R. Niezgoda, Influence of deformation induced nanoscale twinning and FCC-HCP

transformation on hardening and texture development in medium-entropy CrCoNi alloy, Acta Mater. 158 (2018) 38–52.

[74] S. Picak, Deformation Mechanisms in Single Crystalline and Ultrafine Polycrystalline Medium and High Entropy Alloys. Doctoral dissertation, Texas A&M University, (2021).

[75] H. He, M. Naeem, F. Zhang, Y. Zhao, S. Harjo, T. Kawasaki, B. Wang, X. Wu, S. Lan, Z. Wu, W. Yin, Y. Wu, Z. Lu, J.-J. Kai, C.-T. Liu, X.-L. Wang, Stacking Fault Driven Phase Transformation in CrCoNi Medium Entropy Alloy, Nano Lett. 21 (2021) 1419–1426.

[76] R. Su, D. Neffati, Y. Zhang, J. Cho, J. Li, H. Wang, Y. Kulkarni, X. Zhang, The influence of stacking faults on mechanical behavior of advanced materials, Mater. Sci. Eng. A 803 (2021) 140696.

[77] L.-B. Han, Q. An, R.-S. Fu, L. Zheng, S.-N. Luo, Melting of defective Cu with stacking faults, J. Chem. Phys. 130 (2009).

[78] R. Su, D. Neffati, S. Xue, Q. Li, Z. Fan, Y. Liu, H. Wang, Y. Kulkarni, X. Zhang, Deformation mechanisms in FCC Co dominated by high-density stacking faults, Mater. Sci. Eng. A 736 (2018) 12–21.

[79] R. Su, D. Neffati, J. Cho, Q. Li, J. Ding, H. Wang, Y. Kulkarni, X. Zhang, Phase transformation induced plasticity in high-strength hexagonal close packed Co with stacking faults, Scr. Mater. 173 (2019) 32–36.

[80] W.W. Jian, G.M. Cheng, W.Z. Xu, H. Yuan, M.H. Tsai, Q.D. Wang, C.C. Koch, Y.T. Zhu, S.N. Mathaudhu, Ultrastrong Mg alloy via nano-spaced stacking faults, Mater. Res. Lett. 1 (2013) 61–66.

[81] K. Wu, J.Y. Zhang, G. Li, Y.Q. Wang, J.C. Cui, G. Liu, J. Sun, Stacking fault-mediated ultrastrong nanocrystalline Ti thin films, Nanotechnology 28 (2017) 445706.

[82] X. Feng, J. Zhang, K. Wu, X. Liang, G. Liu, J. Sun, Ultrastrong Al0.1CoCrFeNi high-entropy alloys at small scales: Effects of stacking faults: Vs. nanotwins, Nanoscale 10 (2018) 13329–13334.

[83] Z. Li, C.C. Tasan, K.G. Pradeep, D. Raabe, A TRIP-assisted dual-phase high-entropy alloy: Grain size and phase fraction effects on deformation behavior, Acta Mater. 131 (2017) 323–335.

[84] S. Picak, J. Liu, C. Hayrettin, W. Nasim, D. Canadinc, K. Xie, Y.I. Chumlyakov, I. V Kireeva, I. Karaman, Anomalous work hardening behavior of Fe40Mn40Cr10Co10 high entropy alloy single crystals deformed by twinning and slip, Acta Mater. 181 (2019) 555–569.

[85] V. Gerold, H.P. Karnthaler, On the origin of planar slip in f.c.c. alloys, Acta

Metall. 37 (1989) 2177–2183.

[86] F. Pettinari, M. Prem, G. Krexner, P. Caron, A. Coujou, H.O.K. Kirchner, N. Clemént, Local order in industrial and model γ phases of superalloys, Acta Mater. 49 (2001) 2549–2556.

[87] N. Clement, A. Coujou, Y. Calvayrac, F. Guillet, D. Blavette, S. Duval, Local Order and Associated Deformation Mechanisms in the γ Phase of Nickel Base Superalloys, Microsc. Microanal. Microstruct. 7 (1996) 65–84.

[88] J.B. Cohen, M.E. Fine, Some aspects of short-range order, J. Phys. Radium 23 (1962) 749–762.

[89] P. Singh, A. V Smirnov, A. Alam, D.D. Johnson, First-principles prediction of incipient order in arbitrary high-entropy alloys: exemplified in Ti0.25CrFeNiAlx, Acta Mater. 189 (2020) 248–254.

[90] Y. Wu, F. Zhang, X. Yuan, H. Huang, X. Wen, Y. Wang, M. Zhang, H. Wu, X. Liu, H. Wang, S. Jiang, Z. Lu, Short-range ordering and its effects on mechanical properties of high-entropy alloys, J. Mater. Sci. Technol. 62 (2021) 214–220.

[91] B. Schönfeld, C.R. Sax, J. Zemp, M. Engelke, P. Boesecke, T. Kresse, T. Boll, T. Al-Kassab, O.E. Peil, A. V Ruban, Local order in Cr-Fe-Co-Ni: Experiment and electronic structure calculations, Phys. Rev. B 99 (2019) 14206.

[92] A. Fernández-Caballero, J.S. Wróbel, P.M. Mummery, D. Nguyen-Manh, Short-Range Order in High Entropy Alloys: Theoretical Formulation and Application to Mo-Nb-Ta-V-W System, J. Phase Equilibria Diffus. 38 (2017) 391–403.

[93] Y.Y. Shang, Y. Wu, J.Y. He, X.Y. Zhu, S.F. Liu, H.L. Huang, K. An, Y. Chen, S.H. Jiang, H. Wang, X.J. Liu, Z.P. Lu, Solving the strength-ductility tradeoff in the medium-entropy NiCoCr alloy via interstitial strengthening of carbon, Intermetallics 106 (2019) 77–87.

[94] B. Yin, S. Yoshida, N. Tsuji, W.A. Curtin, Yield strength and misfit volumes of NiCoCr and implications for short-range-order, Nat. Commun. 11 (2020) 2507.

[95] S.M. Copley, B.H. Kear, The dependence of the width of a dissociated dislocation on dislocation velocity, Acta Metall. 16 (1968) 227–231.

[96] X. Wu, Chemical short-range orders in high-/medium-entropy alloys, J. Mater. Sci. Technol. 147 (2023) 189–196.

[97] S. Maiti, W. Steurer, Structural-disorder and its effect on mechanical properties in single-phase TaNbHfZr high-entropy alloy, Acta Mater. 106 (2016) 87–97.

[98] R. Zhang, S. Zhao, C. Ophus, Y. Deng, S.J. Vachhani, B. Ozdol, R. Traylor, K.C. Bustillo, J.W. Morris, D.C. Chrzan, M. Asta, A.M. Minor, Direct imaging of short-range order and its impact on deformation in Ti-6Al, Sci. Adv. 5 (2024) eaax2799.

[99] L. Zhou, Q. Wang, J. Wang, X. Chen, P. Jiang, H. Zhou, F. Yuan, X. Wu, Z. Cheng, E. Ma, Atomic-scale evidence of chemical short-range order in CrCoNi medium-entropy alloy, Acta Mater. 224 (2022) 117490.

[100] S. Picak, P. Singh, D. Salas, M.A. Tunes, X. Fang, L. Zhou, M.J. Kramer, Y.I. Chumlyakov, D.D. Johnson, R. Arroyave, Y. Ren, I. Karaman, Orientation dependence of the effect of short-range ordering on the plastic deformation of a medium entropy alloy, Mater. Sci. Eng. A 888 (2023) 145309.

[101] G. Van Tendeloo, S. Amelinckx, The origin of diffuse intensity in electron diffraction patterns, Phase Transitions 67 (1998) 101–135.

[102] D. Liu, Q. Wang, J. Wang, X.F. Chen, P. Jiang, F.P. Yuan, Z.Y. Cheng, E. Ma, X.L. Wu, Chemical short-range order in Fe50Mn30Co10Cr10 high-entropy alloy, Mater. Today Nano 16 (2021) 100139.

[103] J. Wang, P. Jiang, F. Yuan, X. Wu, Chemical medium-range order in a medium-entropy alloy, Nat. Commun. 13 (2022) 1021.

[104] N. Liu, X. Tian, Q. Liu, B. Gan, J. Ding, E. Ma, Z. Wang, Aging elevates chemical short-range order and twinning stress in a CrCoNi medium-entropy alloy, Sci. China Mater. 66 (2023) 4220–4225.

[105] T.J. Ziehl, D. Morris, P. Zhang, Detection and impact of short-range order in medium/high-entropy alloys, IScience 26 (2023) 106209.

[106] A. Marucco, Atomic ordering and α′-Cr phase precipitation in long-term aged Ni3Cr and Ni2Cr alloys, J. Mater. Sci. 30 (1995) 4188–4194.

[107] L. Li, Z. Chen, S. Kuroiwa, M. Ito, K. Yuge, K. Kishida, H. Tanimoto, Y. Yu, H. Inui, E.P. George, Evolution of short-range order and its effects on the plastic deformation behavior of single crystals of the equiatomic Cr-Co-Ni medium-entropy alloy, Acta Mater. 243 (2023) 118537.

[108] J.B. Seol, W.-S. Ko, S.S. Sohn, M.Y. Na, H.J. Chang, Y.-U. Heo, J.G. Kim, H. Sung, Z. Li, E. Pereloma, H.S. Kim, Mechanically derived short-range order and its impact on the multi-principal-element alloys, Nat. Commun. 13 (2022) 6766.

[109] Q.-J. Li, H. Sheng, E. Ma, Strengthening in multi-principal element alloys with local-chemical-order roughened dislocation pathways, Nat. Commun. 10 (2019) 3563.

[110] X. Chen, Q. Wang, Z. Cheng, M. Zhu, H. Zhou, P. Jiang, L. Zhou, Q. Xue, F.

Yuan, J. Zhu, X. Wu, E. Ma, Direct observation of chemical short-range order in a medium-entropy alloy, Nature 592 (2021) 712–716.

[111] B.C. De Cooman, Y. Estrin, S.K. Kim, Twinning-induced plasticity (TWIP) steels, Acta Mater. 142 (2018) 283–362.

[112] C. Liu, W. Lu, W. Xia, C. Du, Z. Rao, J.P. Best, S. Brinckmann, J. Lu, B. Gault, G. Dehm, G. Wu, Z. Li, D. Raabe, Massive interstitial solid solution alloys achieve near-theoretical strength, Nat. Commun. 13 (2022) 1102.

[113] C. Zhu, L. Xu, M. Liu, M. Guo, S. Wei, A review on improving mechanical properties of high entropy alloy: interstitial atom doping, J. Mater. Res. Technol. 24 (2023) 7832–7851.

[114] A. Kumar, A. Singh, A. Suhane, Mechanically alloyed high entropy alloys: existing challenges and opportunities, J. Mater. Res. Technol. 17 (2022) 2431–2456.

[115] H. Conrad, Effect of interstitial solutes on the strength and ductility of titaniums, Prog. Mater. Sci. 26 (1981) 123–403.

[116] J. Svoboda, W. Ecker, V.I. Razumovskiy, G.A. Zickler, F.D. Fischer, Kinetics of interaction of impurity interstitials with dislocations revisited, Prog. Mater. Sci. 101 (2019) 172–206.

[117] I. Gutierrez-Urrutia, D. Raabe, Multistage strain hardening through dislocation substructure and twinning in a high strength and ductile weight-reduced Fe–Mn–Al–C steel, Acta Mater. 60 (2012) 5791–5802.

[118] I. Gutierrez-Urrutia, D. Raabe, Microbanding mechanism in an Fe–Mn–C high-Mn twinning-induced plasticity steel, Scr. Mater. 69 (2013) 53–56.

[119] Z. Wang, I. Baker, Z. Cai, S. Chen, J.D. Poplawsky, W. Guo, The effect of interstitial carbon on the mechanical properties and dislocation substructure evolution in Fe40.4Ni11.3Mn34.8Al7.5Cr6 high entropy alloys, Acta Mater. 120 (2016) 228–239.

[120] L. Guo, X. Ou, S. Ni, Y. Liu, M. Song, Effects of carbon on the microstructures and mechanical properties of FeCoCrNiMn high entropy alloys, Mater. Sci. Eng. A 746 (2019) 356–362.

[121] P. Cui, Y. Ma, L. Zhang, M. Zhang, J. Fan, W. Dong, P. Yu, G. Li, R. Liu, Effect of Ti on microstructures and mechanical properties of high entropy alloys based on CoFeMnNi system, Mater. Sci. Eng. A 737 (2018) 198–204.

[122] Y. CHEN, J. Tu, Y. Zhang, L. Tan, R. Yin, Z. ZHOU, Effect of Deformation and Annealing Process on Microstructural Evolution of Fe47Mn30Co10Cr10B3 High Entropy Alloy, Chinese J. Mater. Res. 35 (2021) 143–153.

[123] F.M. BAI Li, WANG Yuzhe, LYU Yukun, YAN Yi, Effect of Carbon on Microstructures and Mechanical Properties of Co-free Fe40Mn30Ni10Cr10Al10 High-entropy Alloy, Mater. Reports 34 (2020) 17072–17076.

[124] L.B. Chen, R. Wei, K. Tang, J. Zhang, F. Jiang, L. He, J. Sun, Heavy carbon alloyed FCC-structured high entropy alloy with excellent combination of strength and ductility, Mater. Sci. Eng. A 716 (2018) 150–156.

[125] M. Traversier, P. Mestre-Rinn, N. Peillon, E. Rigal, X. Boulnat, F. Tancret, J. Dhers, A. Fraczkiewicz, Nitrogen-induced hardening in an austenitic CrFeMnNi high-entropy alloy (HEA), Mater. Sci. Eng. A 804 (2021) 140725.

[126] L. ZHANG, R. SONG, G. QU, T. LU, Effect of nitrogen on microstructure and mechanical properties of CrMnFeVTi6 high entropy alloy, Trans. Nonferrous Met. Soc. China 31 (2021) 2415–2427.

[127] Y. Xie, H. Cheng, Q. Tang, W. Chen, W. Chen, P. Dai, Effects of N addition on microstructure and mechanical properties of CoCrFeNiMn high entropy alloy produced by mechanical alloying and vacuum hot pressing sintering, Intermetallics 93 (2018) 228–234.

[128] I. Moravcik, H. Hadraba, L. Li, I. Dlouhy, D. Raabe, Z. Li, Yield strength increase of a CoCrNi medium entropy alloy by interstitial nitrogen doping at maintained ductility, Scr. Mater. 178 (2020) 391–397.

[129] D.E. Jodi, J. Park, N. Park, Strengthening of ultrafine-grained equiatomic CoCrFeMnNi high-entropy alloy by nitrogen addition, Mater. Lett. 258 (2020) 126772.

[130] K.H. Lo, C.H. Shek, J.K.L. Lai, Recent developments in stainless steels, Mater. Sci. Eng. R Reports 65 (2009) 39–104.

[131] B.J. Lee, J.S. Song, W.J. Moon, S.I. Hong, Modifications of partial-dislocation-induced defects and strength/ductility enhancement in metastable high entropy alloys through nitrogen doping, Mater. Sci. Eng. A 803 (2021) 140684.

[132] Y. Han, H. Li, H. Feng, K. Li, Y. Tian, Z. Jiang, Enhancing the strength and ductility of CoCrFeMnNi high-entropy alloy by nitrogen addition, Mater. Sci. Eng. A 789 (2020) 139587.

[133] W. Li, P. Liu, P.K. Liaw, Microstructures and properties of high-entropy alloy films and coatings: a review, Mater. Res. Lett. 6 (2018) 199–229.

[134] R. Chen, Z. Cai, J. Pu, Z. Lu, S. Chen, S. Zheng, C. Zeng, Effects of nitriding on the microstructure and properties of VAlTiCrMo high-entropy alloy coatings by sputtering technique, J. Alloys Compd. 827 (2020) 153836.

[135] K.-H. Cheng, C.-H. Lai, S.-J. Lin, J.-W. Yeh, Structural and mechanical properties of multi-element (AlCrMoTaTiZr)Nx coatings by reactive magnetron sputtering, Thin Solid Films 519 (2011) 3185–3190.

[136] B. Barkia, V. Doquet, J.P. Couzinié, I. Guillot, E. Héripré, In situ monitoring of the deformation mechanisms in titanium with different oxygen contents, Mater. Sci. Eng. A 636 (2015) 91–102.

[137] Q. Yu, L. Qi, T. Tsuru, R. Traylor, D. Rugg, J.W. Morris, M. Asta, D.C. Chrzan, A.M. Minor, Origin of dramatic oxygen solute strengthening effect in titanium, Science (80-.). 347 (2015) 635–639.

[138] Z. Liu, G. Welsch, Effects of oxygen and heat treatment on the mechanical properties of alpha and beta titanium alloys, Metall. Trans. A 19 (1988) 527–542.

[139] W.U. Zeen, H.U. Rui, Z. Tiebang, Z. Huan, K. Hongchao, L.I. Jinshan, EFFECT OF OXYGEN ON MICROSTRUCTURE AND PHASE TRANSFORMATION OF HIGH Nb CONTAINING TiAl ALLOYS, Acta Met. Sin 49 (2013) 1381–1386.

[140] J. Wadsworth, T.G. Nieh, J.J. Stephens, Recent advances in aerospace refractory metal alloys, Int. Mater. Rev. 33 (1988) 131–150.

[141] Y. Wu, Q. Wang, D. Lin, X. Chen, T. Wang, W.Y. Wang, Y. Wang, X. Hui, Phase Stability and Deformation Behavior of TiZrHfNbO High-Entropy Alloys, Front. Mater. 7 (2020).

[142] C. Ghosh, A. Singh, J. Basu, D. Ramachandran, E. Mohandas, Microstructural and microchemical studies of phase stability in V-O solid solution, Mater. Charact. 124 (2017) 129–135.

[143] Y. Chen, Y. Li, X. Cheng, Z. Xu, C. Wu, B. Cheng, M. Wang, Interstitial strengthening of refractory ZrTiHfNb0.5Ta0.5Ox (x = 0.05, 0.1, 0.2) high-entropy alloys, Mater. Lett. 228 (2018) 145–147.

[144] L.S. Wei, H.Y. Kim, T. Koyano, S. Miyazaki, Effects of oxygen concentration and temperature on deformation behavior of Ti-Nb-Zr-Ta-O alloys, Scr. Mater. 123 (2016) 55–58.

[145] Z. Lei, X. Liu, Y. Wu, H. Wang, S. Jiang, S. Wang, X. Hui, Y. Wu, B. Gault, P. Kontis, D. Raabe, L. Gu, Q. Zhang, H. Chen, H. Wang, J. Liu, K. An, Q. Zeng, T.-G. Nieh, Z. Lu, Enhanced strength and ductility in a high-entropy alloy via ordered oxygen complexes, Nature 563 (2018) 546–550.

[146] R.O. Ritchie, The conflicts between strength and toughness, Nat. Mater. 10 (2011) 817–822.

[147] D. Xu, X. Wang, Y. Lu, Heterogeneous-Structured Refractory High-Entropy

Alloys: A Review of State-of-the-Art Developments and Trends, Adv. Funct. Mater. n/a (2024) 2408941.

[148] Y. Horiuchi, T. Inamura, H. Hosoda, K. Wakashima, H.Y. Kim, S. Miyazaki, Effect of boron addition on transformation behavior and tensile properties of Ti–Nb–Al alloy, Mater. Sci. Eng. A 438–440 (2006) 830–834.

[149] D. Tytko, P.-P. Choi, J. Klöwer, A. Kostka, G. Inden, D. Raabe, Microstructural evolution of a Ni-based superalloy (617B) at 700°C studied by electron microscopy and atom probe tomography, Acta Mater. 60 (2012) 1731–1740.

[150] Y. Jiang, X.M. Li, G.T. Zhou, B.X. Zhu, Effects of B content on microstructure and properties of CrFeCoNiTi0. 6 high-entropy alloy, Mater. Sci. Eng. Powder Met. 25 (2020) 403–409.

[151] L. Hou, J. Hui, Y. Yao, J. Chen, J. Liu, Effects of Boron Content on microstructure and mechanical properties of AlFeCoNiBx High Entropy Alloy Prepared by vacuum arc melting, Vacuum 164 (2019) 212–218.

[152] Y. Shi, Y.-D. Wang, S. Li, R. Li, Y. Wang, Mechanical behavior in boron-microalloyed CoCrNi medium-entropy alloy studied by in situ high-energy X-ray diffraction, Mater. Sci. Eng. A 788 (2020) 139600.

[153] R.W. Cahn, P. Haasen, E.J. Kramer, Materials science and technology: A comprehensive treatment, in: 2001.

[154] The World Book Encyclopedia, W-X-Y-Z, in: 1973: p. 501.

[155] Dbuckingham, Wikpedia, (2017).

[156] J.H. Wernick, Determination of Diffusivities in Liquid Metals by Means of Temperature-Gradient Zone Melting, J. Chem. Phys. 25 (1956) 47–49.

[157] W.G. Pfann, Techniques of Zone Melting and Crystal Growing, in: F. SEITZ, D.B.T.-S.S.P. TURNBULL (Eds.), Academic Press, 1957: pp. 423–521.

[158] P. Rudolph, Handbook of Crystal Growth: Bulk Crystal Growth, Elsevier Science, 2014.

[159] V.E. Gromov, S. V Konovalov, Y.F. Ivanov, K.A. Osintsev, Methods of Manufacturing the High-Entropy Alloys BT - Structure and Properties of High-Entropy Alloys, in: V.E. Gromov, S. V Konovalov, Y.F. Ivanov, K.A. Osintsev (Eds.), Springer International Publishing, Cham, 2021: pp. 1–31.

[160] T. Nishinaga, Handbook of Crystal Growth: Fundamentals, Elsevier Science, 2014.

[161] P. Capper, P. Rudolph, Crystal Growth Technology: Semiconductors and Dielectrics, 2010.

[162] P. Capper, Semiconductor Electrochemistry., 2010.

[163] R. Feigelson, Crystal Growth through the Ages, in: 2015: pp. 1–83.

[164] P. Rudolph, F. Kiessling, The horizontal bridgman method, Cryst. Res. Technol. 23 (1988) 1207–1224.

[165] I. Elswie, Z. Lazarevic, V. Radojevic, M. Gilic, M. Rabasovic, D. Sevic, N. Romcevic, The Bridgman method growth and spectroscopic characterization of calcium fluoride single crystals, Sci. Sinter. 48 (2016) 333–341.

[166] D. Ma, Novel casting processes for single-crystal turbine blades of superalloys, Front. Mech. Eng. 13 (2017).

[167] X. Li, E. Ruckenstein, Chemical Vapor Deposition (CVD) Encyclopedia of Surface and Colloid Science, (1993).

[168] R. Lewis, Principles of Chemical Vapor Deposition. Kluwer Academic Publishers, (1996).

[169] Y. Xu, X. Yan, Chemical Vapour Deposition: An Integrated Engineering Design for Advanced Materials, in: 2010.

[170] D.M. Mattox, Physical Vapor Deposition (PVD) Processing, Elsevier Science, 2010.

[171] K.K. Schuegraf, Thin-film Deposition Processes and Techniques: Principles, Methods, Equipment, and Applications, Noyes Publications, 1988.

[172] C.B. Carter, M.G. Norton, Ceramic Materials: Science and Engineering, Springer New York, 2007.

[173] C.B. Carter, M.G. Norton, eds., Growing Single Crystals BT - Ceramic Materials: Science and Engineering, in: Springer New York, New York, NY, 2007: pp. 507–526.

[174] B. Schuh, F. Mendez-Martin, B. Völker, E.P. George, H. Clemens, R. Pippan, A. Hohenwarter, Mechanical properties, microstructure and thermal stability of a nanocrystalline CoCrFeMnNi high-entropy alloy after severe plastic deformation, Acta Mater. 96 (2015) 258–268.

[175] H. Shahmir, J. He, Z. Lu, M. Kawasaki, T.G. Langdon, Effect of annealing on mechanical properties of a nanocrystalline CoCrFeNiMn high-entropy alloy processed by high-pressure torsion, Mater. Sci. Eng. A 676 (2016) 294–303.

[176] S. Yoshida, T. Bhattacharjee, Y. Bai, N. Tsuji, Friction stress and Hall-Petch relationship in CoCrNi equi-atomic medium entropy alloy processed by severe plastic deformation and subsequent annealing, Scr. Mater. 134 (2017) 33–36.

[177] B. Schuh, R. Pippan, A. Hohenwarter, Tailoring bimodal grain size structures in nanocrystalline compositionally complex alloys to improve ductility, Mater. Sci. Eng. A 748 (2019) 379–385.

[178] H. Shahmir, T. Mousavi, J. He, Z. Lu, M. Kawasaki, T.G. Langdon, Microstructure and properties of a CoCrFeNiMn high-entropy alloy processed by equal-channel angular pressing, Mater. Sci. Eng. A 705 (2017) 411–419.

[179] H.W. Deng, Z.M. Xie, B.L. Zhao, Y.K. Wang, M.M. Wang, J.F. Yang, T. Zhang, Y. Xiong, X.P. Wang, Q.F. Fang, C.S. Liu, Tailoring mechanical properties of a CoCrNi medium-entropy alloy by controlling nanotwin-HCP lamellae and annealing twins, Mater. Sci. Eng. A 744 (2019) 241–246.

[180] P. Yu, L. Zhang, H. Cheng, H. Tang, J. Fan, P.K. Liaw, G. Li, R. Liu, Formation, reverse transformation, and properties of ε-martensite phase in the CoCrFeMnNi high-entropy alloy under high-pressure, J. Alloys Compd. 779 (2019) 1–6.

[181] D.-H. Lee, I.-C. Choi, M.-Y. Seok, J. He, Z. Lu, J.-Y. Suh, M. Kawasaki, T.G. Langdon, J. Jang, Nanomechanical behavior and structural stability of a nanocrystalline CoCrFeNiMn high-entropy alloy processed by high-pressure torsion, J. Mater. Res. 30 (2015) 2804–2815.

[182] W. Skrotzki, A. Pukenas, E. Odor, B. Joni, T. Ungar, B. Völker, A. Hohenwarter, R. Pippan, E.P. George, Microstructure, Texture, and Strength Development during High-Pressure Torsion of CrMnFeCoNi High-Entropy Alloy, Crystals 10 (2020).

[183] T. Niendorf, F. Rubitschek, H.J. Maier, J. Niendorf, H.A. Richard, A. Frehn, Fatigue crack growth—Microstructure relationships in a high-manganese austenitic TWIP steel, Mater. Sci. Eng. A 527 (2010) 2412–2417.

[184] C.W. Shao, P. Zhang, R. Liu, Z.J. Zhang, J.C. Pang, Q.Q. Duan, Z.F. Zhang, A remarkable improvement of low-cycle fatigue resistance of high-Mn austenitic TWIP alloys with similar tensile properties: Importance of slip mode, Acta Mater. 118 (2016) 196–212.

[185] J.T.P., Yao, W.H. Munse, Low-cycle fatigue behavior of axially loaded specimens of mild steel, (1962).

[186] B. Haghgouyan, B. Young, S. Picak, T. Baxevanis, I. Karaman, D.C. Lagoudas, A unified description of mechanical and actuation fatigue crack growth in shape memory alloys, Acta Mater. 217 (2021) 117155.

[187] D. An, W. Krieger, S. Zaefferer, Unravelling the effect of hydrogen on microstructure evolution under low-cycle fatigue in a high-manganese austenitic TWIP steel, Int. J. Plast. 126 (2020) 102625.

[188] A.S. Hamada, L.P. Karjalainen, J. Puustinen, Fatigue behavior of high-Mn TWIP steels, Mater. Sci. Eng. A 517 (2009) 68–77.

[189] T. Niendorf, C. Lotze, D. Canadinc, A. Frehn, H.J. Maier, The role of monotonic pre-deformation on the fatigue performance of a high-manganese austenitic TWIP steel, Mater. Sci. Eng. A 499 (2009) 518–524.

[190] C.W. Shao, P. Zhang, R. Liu, Z.J. Zhang, J.C. Pang, Z.F. Zhang, Low-cycle and extremely-low-cycle fatigue behaviors of high-Mn austenitic TRIP/TWIP alloys: Property evaluation, damage mechanisms and life prediction, Acta Mater. 103 (2016) 781–795.

[191] K. Liu, M. Komarasamy, B. Gwalani, S. Shukla, R.S. Mishra, Fatigue behavior of ultrafine grained triplex Al0.3CoCrFeNi high entropy alloy, Scr. Mater. 158 (2019) 116–120.

[192] Y.Z. Tian, S.J. Sun, H.R. Lin, Z.F. Zhang, Fatigue behavior of CoCrFeMnNi high-entropy alloy under fully reversed cyclic deformation, J. Mater. Sci. Technol. 35 (2019) 334–340.

[193] M.A. Hemphill, T. Yuan, G.Y. Wang, J.W. Yeh, C.W. Tsai, A. Chuang, P.K. Liaw, Fatigue behavior of Al0.5CoCrCuFeNi high entropy alloys, Acta Mater. 60 (2012) 5723–5734.

[194] K. Liu, S.S. Nene, M. Frank, S. Sinha, R.S. Mishra, Extremely high fatigue resistance in an ultrafine grained high entropy alloy, Appl. Mater. Today 15 (2019) 525–530.

[195] F. Bahadur, K. Biswas, N.P. Gurao, Micro-mechanisms of microstructural damage due to low cycle fatigue in CoCuFeMnNi high entropy alloy, Int. J. Fatigue 130 (2020) 105258.

[196] T. Niendorf, T. Wegener, Z. Li, D. Raabe, Unexpected cyclic stress-strain response of dual-phase high-entropy alloys induced by partial reversibility of deformation, Scr. Mater. 143 (2018) 63–67.

[197] S. Picak, T. Wegener, S.V. Sajadifar, C. Sobrero, J. Richter, H. Kim, T. Niendorf, I. Karaman, On the low-cycle fatigue response of CoCrNiFeMn high entropy alloy with ultra-fine grain structure, Acta Mater. 205 (2021) 116540.

[198] T. Niendorf, D. Canadinc, H.J. Maier, Fatigue Damage Evolution in Ultrafine-Grained Interstitial-Free Steel, Adv. Eng. Mater. 13 (2011) 275–280.

[199] S. V Sajadifar, T. Wegener, G.G. Yapici, T. Niendorf, Effect of grain size on the very high cycle fatigue behavior and notch sensitivity of titanium, Theor. Appl. Fract. Mech. 104 (2019) 102362.

[200] I.P. Semenova, G.K. Salimgareeva, V. V Latysh, T. Lowe, R.Z. Valiev, Enhanced fatigue strength of commercially pure Ti processed by severe plastic

deformation, Mater. Sci. Eng. A 503 (2009) 92–95.

[201] H.J. Maier, P. Gabor, N. Gupta, I. Karaman, M. Haouaoui, Cyclic stress–strain response of ultrafine grained copper, Int. J. Fatigue 28 (2006) 243–250.

[202] T. Niendorf, D. Canadinc, H.J. Maier, I. Karaman, G.G. Yapici, Microstructure–mechanical property relationships in ultrafine-grained NbZr, Acta Mater. 55 (2007) 6596–6605.

[203] T. Niendorf, D. Canadinc, H.J. Maier, I. Karaman, The role of heat treatment on the cyclic stress–strain response of ultrafine-grained interstitial-free steel, Int. J. Fatigue 30 (2008) 426–436.

[204] H.W. Höppel, M. Kautz, C. Xu, M. Murashkin, T.G. Langdon, R.Z. Valiev, H. Mughrabi, An overview: Fatigue behaviour of ultrafine-grained metals and alloys, Int. J. Fatigue 28 (2006) 1001–1010.

[205] L. Kunz, P. Lukáš, M. Svoboda, Fatigue strength, microstructural stability and strain localization in ultrafine-grained copper, Mater. Sci. Eng. A 424 (2006) 97–104.

[206] T. Niendorf, D. Canadinc, H.J. Maier, I. Karaman, On the Microstructural Stability of Ultrafine-Grained Interstitial-Free Steel under Cyclic Loading, Metall. Mater. Trans. A 38 (2007) 1946–1955.

[207] T. Niendorf, J. Dadda, D. Canadinc, H.J. Maier, I. Karaman, Monitoring the fatigue-induced damage evolution in ultrafine-grained interstitial-free steel utilizing digital image correlation, Mater. Sci. Eng. A 517 (2009) 225–234.

[208] L. Collini, Fatigue crack growth in ECAPed commercially pure UFG copper, Procedia Eng. 2 (2010) 2065–2074.

[209] T. Niendorf, F. Rubitschek, H.J. Maier, D. Canadinc, I. Karaman, On the fatigue crack growth–microstructure relationship in ultrafine-grained interstitial-free steel, J. Mater. Sci. 45 (2010) 4813–4821.

[210] H.J. Maier, P. Gabor, I. Karaman, Cyclic stress–strain response and low-cycle fatigue damage in ultrafine grained copper, Mater. Sci. Eng. A 410–411 (2005) 457–461.

[211] J. May, D. Amberger, M. Dinkel, H.W. Höppel, M. Göken, Monotonic and cyclic deformation behaviour of ultrafine-grained aluminium, Mater. Sci. Eng. A 483–484 (2008) 481–484.

[212] D. Canadinc, T. Niendorf, H.J. Maier, A comprehensive evaluation of parameters governing the cyclic stability of ultrafine-grained FCC alloys, Mater. Sci. Eng. A 528 (2011) 6345–6355.

[213] K. Hockauf, M.F.-X. Wagner, T. Halle, T. Niendorf, M. Hockauf, T. Lampke,

Influence of precipitates on low-cycle fatigue and crack growth behavior in an ultrafine-grained aluminum alloy, Acta Mater. 80 (2014) 250–263.

[214] T. Niendorf, H.J. Maier, D. Canadinc, I. Karaman, Cyclic stability of ultrafine-grained interstitial-free steel at elevated temperatures, Mater. Sci. Eng. A 503 (2009) 160–162.

[215] S. V Sajadifar, G.G. Yapici, E. Demler, P. Krooß, T. Wegener, H.J. Maier, T. Niendorf, Cyclic deformation response of ultra-fine grained titanium at elevated temperatures, Int. J. Fatigue 122 (2019) 228–239.

[216] S. Picak, Deformation Mechanisms in Single Crystalline and Ultrafine Polychrystalline Medium and High Entropy Alloys, Texas A&M University, 2021.

[217] I. Karaman, H. Sehitoglu, H.J. Maier, Y.I. Chumlyakow, Competing mechanisms and modeling of deformation in austenitc stainless single cystals with and without nitrogen, Acta Mater. 49 (2001) 3919–3933.

[218] I. Karaman, H.. Sehitoglu, HMaier, K. Gall, Y.. Chumlyakov, Deformation of single crystal Hadfield steel by twinning and slip, Acta Mater. 48 (2002) 1345–1359.

[219] I. Karaman, H. Sehitoglu, Y.I. Chumlyakov, H.J. Maier, I. V Kireeva, The Effect of twinning and slip on the bauschinger effect of hadfield steel single crystals, Metall. Mater. Trans. A 32 (2001) 695–706.

[220] I. Karaman, H. Sehitoglu, Y.I. Chumlyakov, H.J. Maier, I.V. Kireeva, Extrinsic stacking faults and twinning in Hadfield manganese steel single crystals, Scr. Mater. 44 (2001) 337–343.

[221] D. Canadinc, H. Sehitoglu, H.J. Maier, Y.I. Chumlyakov, Strain hardening behavior of aluminum alloyed Hadfield steel single crystals, Acta Mater. 53 (2005) 1831–1842.

[222] L. Patriarca, A. Ojha, H. Sehitoglu, Y.I. Chumlyakov, Slip nucleation in single crystal FeNiCoCrMn high entropy alloy, Scr. Mater. 112 (2016) 54–57.

[223] D. Canadinc, I. Karaman, Y. Chumlyakov, The Role of Nitrogen on the Deformation Response of Hadfield Steel Single Crystals, Metall. Mater. Trans. A 34 (9) (2003).

[224] I. Karaman, H. Sehitoglu, Y.I. Chumlyakov, H.J. Maier, The deformation of low-stacking- fault-energy austenitic steels, 54 (2002) 31–37.

[225] S. Asgari, E. El-Danaf, S.R. Kalidindi, R.D. Doherty, Strain hardening regimes and microstructural evolution during large strain compression of low stacking fault energy fcc alloys that form deformation twins, Metall. Mater. Trans. A 28 (1997) 1781–1795.

[226] F. Pettinari, M. Prem, G. Krexner, P. Caron, A. Coujou, H.O.K. Kirchner, N. Clemént, Local order in industrial and model γ phases of superalloys, Acta Mater. 49 (2001) 2549–2556.

[227] V. Gerold, H.P. Karnthaler, On the origin of planar slip in f.c.c. alloys, Acta Metall. 37 (1989) 2177–2183.

RESUME

Ahmad MADKHANAH, Mechanical Engineering graduate from Karabük University, pursuing a Master's degree in Mechanical Engineering also at Karabük University, expected to graduate in 2024. Highly self-motivated and organized engineer with passion for discovering, learning and developing.